POLITECNICO DI TORINO

Master's Degree in Ingegneria Energetica e Nucleare
Sustainable Nuclear Energy

Master's Degree Thesis

SOLPS-ITER modelling of plasma discharges in Magnum-PSI with a Lithium Vapor Box Divertor Module

Supervisors

Prof. Giuseppe F. NALLO

Prof. Hugo DE BLANK

Prof. Fabio SUBBA

Candidate

Alessio VILLA

March 2024

Abstract

Power exhaust is among the main challenges in the field of nuclear fusion, primarily due to the high heat fluxes associated to charged particles impinging on the walls of fusion reactors. The divertor, a crucial fusion reactor component, plays a key role in exhausting the power generated by fusion reactions occurring in the core plasma. Over the last decades, various divertor configurations have been proposed, and numerous experimental campaigns have been conducted to demonstrate their feasibility in addressing this challenge. In this thesis, the attention will be focused on a particular divertor technology which takes advantage of liquid metals, the so-called Liquid Metal Divertor (LMD). Specifically, a Vapor Box Divertor (VBD) configuration is analysed. This divertor layout, which exploits liquid lithium, is based on the use of different chambers that aim to concentrate a large density of Li vapor in the proximity of the divertor targets, leading to a significant energy and momentum transfer, hence lowering heat and particle loads to the divertor targets themselves. The capability to reduce particle and heat fluxes allows, e.g., to decrease thermo-mechanical stresses, so leading to a longer lifetime of the component.

Although simulations indicate that the VBD can represent a viable solution to the power exhaust problem, dedicated experiments are essential to validate this concept and to assess the predictive capabilities of these simulations. Linear plasma devices (LPDs), such as Magnum-PSI, are indispensable in this context as they are capable of reproducing density, temperature, heat, and particle fluxes characteristic of the Scrape-Off Layer (SOL) region in future fusion reactors. As for the simulations, one of the state-of-the-art tools is represented by the SOLPS-ITER code, which computes the edge and SOL plasma behaviour accounting for the many complex phenomena taking place therein, including the plasma interaction with reactor walls and, for the LMD case, with liquid metal particles. SOLPS-ITER couples a fluid model for the plasma, based on the Braginskii's equations, and a kinetic transport model for neutral particles via the Monte Carlo method.

The present thesis focuses on the modelling of a lithium Vapor Box Module (VBM) within the Magnum-PSI linear plasma device, exploiting the capabilities of the SOLPS-ITER code, which enables to reproduce the complex interactions between lithium and plasma particles. The VBM was conceived in similarity to the actual VBD, hence it aims at generating a dense lithium cloud that effectively reduces heat and particle loads on the target surface by increasing collision processes. Simulations were conducted to investigate two distinct scenarios of the VBM, with and without the presence of lithium, aimed at understanding the impact of the

metal vapor on the plasma beam. By comparing these two cases, the effectiveness of lithium in mitigating heat and particle loads on the Magnum-PSI target is demonstrated. Furthermore, the preparation of the corresponding validation case, based on recent experimental results, is provided.

Acknowledgements

"Per adesso, questo è quello che sappiamo della materia. Una manciata di tipi di particelle elementari, che vibrano e fluttuano in continuazione fra l'esistere e il non esistere, pullulano nello spazio anche quando sembra non ci sia nulla, si combinano assieme all'infinito come le venti lettere di un alfabeto cosmico per raccontare l'immensa storia delle galassie, delle stelle innumerevoli, dei raggi cosmici, della luce del sole, delle montagne, dei boschi, dei campi di grano, dei sorrisi dei ragazzi alle feste, e del cielo nero e stellato la notte."
Carlo Rovelli, Sette brevi lezioni di fisica

Forse è questa una delle parti più complicate della stesura della tesi. Sono stati anni molto intensi, vivi ed emozionanti. Non avrei mai pensato di poter incontrare così tanti compagni di viaggio che, uniti a quelli che sono sempre stati al mio fianco, hanno rallegrato, alleggerito e vivacizzato ogni istante. Sono estramemente grato di tutto questo e credo fortemente che i ringraziamenti non possano mai essere abbastanza.
Vorrei ringraziare la mia famiglia, a partire dai miei genitori, Fabio e Cristina. Mi avete sempre sostenuto, supportato, ascoltato e, diciamoci la verità, anche mantenuto. Spero di assomigliare a voi e di avere la vostra stessa pazienza quando sarò *grande*. Un ringraziamento anche ad Asia, non parliamo tanto, giusto pochissime parole, ma è grazie a te se ho imparato a prendere certe situazioni con maggiore leggerezza. Grazie a nonna Ella e nonna Emma, sempre disponibili a cucinare qualsiasi pietanza e a sfornare preziosi consigli. Grazie a nonno Mario, riferimento speciale nel corso di tutta la mia vita, devo a te la mia curiosità e il mio interesse per le materie scientifiche. Mi hai istruito fin da bambino con le tue storie e sei sempre stato un modello a cui ambire con la tua costante simpatia e spensieratezza. Voglio bene a tutti voi.
Grazie a tutti i miei amici, ho preso il meglio da ognuno di voi. Grazie agli amici di sempre con cui ho vissuto la piccolà realtà di Ovada e con cui sono cresciuto. Con voi ho condiviso risate, storie, emozioni e mi avete regalato momenti di cui non mi dimenticherò mai. Ho apprezzato ogni singolo istante in vostra compagnia, dalle pigre serate all'Enal alle vacanze estive impossibili da organizzare. Spero di rivivere tutto questo, sempre.
Grazie agli amici di Torino, vi ho conosciuto tramite l'università e con voi ho condiviso le bellezze di questa splendida città creando un legame indissolubile. Dalla disperazione dovuta agli esami all'euforia delle Panche, devo dire di essermi divertito, molto.
Vorrei ringraziare anche il prof. Giuseppe Francesco Nallo. Grazie per la pazienza e l'educazione che hai sempre mostrato nei miei confronti, mi hai guidato nel corso di questa tesi fornendo preziose nozioni e consigli fondamentali. Il mio interesse per il mondo della ricerca deriva anche dalla passione che trasmetti.
Non so cosa mi riserverà il futuro, ma fino ad ora credo di non aver mai desiderato nulla di migliore. Grazie a tutti.

Table of Contents

List of Figures

Chapter 1

Introduction

The global energy landscape is characterised by a growing need for a clean energy source which has no impact on the environment in terms of CO_2 emission. The dominant reliance on fossil fuels, such as coal, oil, and natural gas, for energy generation has brought about environmental and geopolitical issues resulting in a recent instability of the energy field. The release of greenhouse gases into the atmosphere has driven climate change, leading to more frequent and severe weather events, so finding a zero carbon energy solution is an essential task. One of the best promising solution is represented by nuclear energy, indeed both fission and fusion could meet the requirements listed before in order to guarantee a zero emissions future energy landscape.

1.1 Nuclear energy

Before moving into the description of nuclear fusion energy details, it is important to explain the physics of nuclear reactions starting from a crucial property: the binding energy. The trend of the specific binding energy, so the binding energy divided by the total number of nucleons, as a function of the mass number A can be seen in figure 1.1. Binding energy E_b corresponds to the minimum amount of energy required to split an atomic nucleus into its components, so nucleons (protons and neutrons), when they are infinitely distant.

$$m(Z,A) + \frac{E_b(Z,A)}{c^2} = Zm_p + (A-Z)m_n \tag{1.1}$$

It is the energy equivalent of the mass defect, so the difference in mass between the nucleus and the sum of its constituents.
Binding energy trend could be explained by the Weizsascker formula:

$$E_b(Z,A) = a_v A - a_s A^{2/3} - a_c \frac{Z^2}{A^{1/3}} - a_{sym}\frac{(N-Z)^2}{A} + \delta(Z,A) \tag{1.2}$$

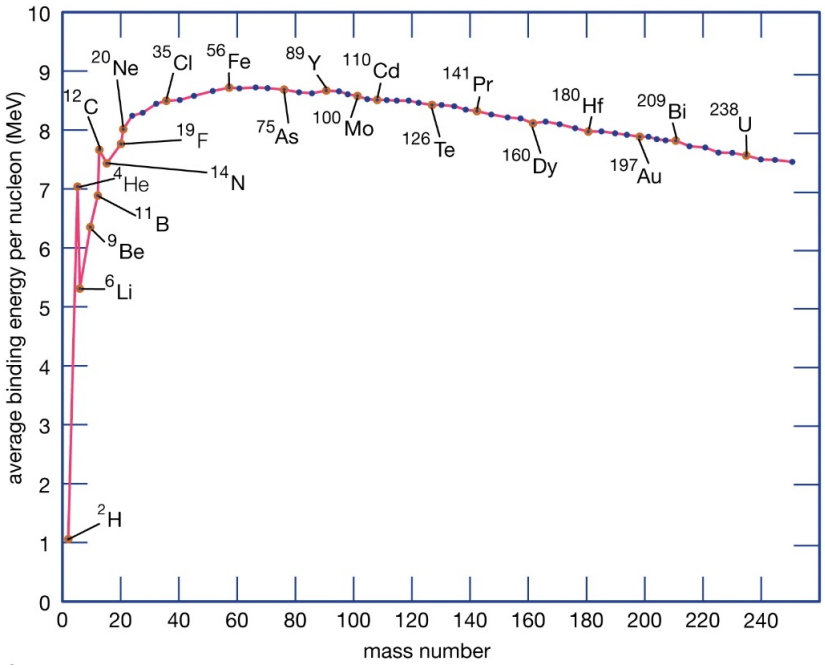

Figure 1.1: Average binding energy per nucleon as a function of the mass number A [1].

In this context, making a distinction between two different types of nucleons is fundamental, indeed nuclei components can be divided into inner nucleons and surface nucleons. All of them interact with nearby nucleons thanks to the strong nuclear force, which has a short range of interaction, but surface nucleons can interact with a lower number of particles, so they are extracted from the nucleus more easily with respect to the inner ones. Having set this, the binding energy can be considered, as a first approximation, proportional to the mass number A. This results in two different terms in the Weizsacker formulation: a volume term, related to the inner nucleons, and a surface term, linked to the surface nucleons. This last term is one of the responsible for the decreasing trend of the binding energy, as it is negative.
Summarising, binding energy firstly increases due to the formation of nuclear bonds between nucleons. This process lasts until the Fe-56 nucleus is reached, then the greater number of nucleons present in the surface, related to weaker bonds, starts playing an important role because surface nucleons are extracted more facilely, and this results in a reduction of the binding energy. Higher mass number implies a greater number of protons. Therefore, for A bigger than 56, the Coulomb repulsion force due to protons positive charge must be taken into account. This is related to a further reduction of the binding energy, as it can be seen in the Weizsascker

formula.
The other components of (1.2) are the symmetry term and the pairing term. The first term is linked to the difference between the atomic number Z and the neutron number N and it increases proportionally to $(N - Z)^2$ determining a reduction of the binding energy. The latter term depends on Z and A and it changes according to the value of the mass number (even or odd). Thus, the binding energy has higher values for nuclei with low mass numbers (< 56) and it begins to decrease for mass numbers bigger than 56. This characteristic is significant because it shows how nuclear fission and nuclear fusion reactions are able to produce energy.
In a nuclear fission reaction, a heavy nucleus (like $U - 235$) is split into two components releasing a great amount of energy after the interaction with a neutron. This process can generate energy due to the mass defect. A heavy nucleus, located in the last part of the binding energy curve, is divided into two different nuclei with a smaller mass number, so related to higher values of the binding energy. The starting element has a lower binding energy with respect to the resulting ones, meaning that a certain amount of energy, equal to the binding one, is released according to Einstein's law.

$$^{235}U + n \rightarrow {}^{142}Ba + {}^{92}Kr + 3n \tag{1.3}$$

In a nuclear fusion reaction, two light nuclei merge to form a single heavier nucleus. Also in this case, the product of the reaction has a higher value of binding energy compared to the two initial nuclei, so this process results in a release of energy, equivalent to the mass defect multiplied by the square of the speed of light. This last quantity corresponds to the binding energy.

1.2 Nuclear fusion reaction

Since the Coulomb barrier is proportional to the square of the atomic number Z, only light nuclei can undergo a nuclear fusion reaction.
The possible reaction types involving hydrogen isotopes and helium are listed below:

$$D + T \rightarrow n + {}^{4}He + 17.6MeV \tag{1.4}$$

$$D + {}^{3}He \rightarrow {}^{4}He + H + 18.3MeV \tag{1.5}$$

$$D + D \rightarrow \begin{cases} {}^{3}He + n + 3.27MeV \\ T + H + 4.03MeV \end{cases} \tag{1.6}$$

There are two fundamental quantities that characterise a nuclear fusion reaction: the reaction rate and the microscopic cross-section. By observing these parameters, it is possible to determine which reaction is the most promising.

The microscopic cross-section is indicated with σ and is related to the probability that a reaction could take place. Its unit of measurement is that of an area and it can be thought of as the target size that a particle must hit in order to generate the nuclear fusion process. Starting from σ, the reaction rate R can be defined as:

$$R = n_i n_j \langle \sigma v \rangle_{ij} \tag{1.7}$$

where n_i and n_j are the density of the species i and j, v is the collision process velocity and $\langle * \rangle$ indicates the average on the velocity distribution. Looking at the cross-section trend (figure 1.2), it is possible to notice that the energy of the particles involved in the reaction has to be high enough in order to deal with a cross-section which is sufficiently large, allowing the nuclear fusion process. Moreover, the rate coefficient $\langle \sigma v \rangle$ must show a similar behaviour (figure 1.3).

The $D - D$ reaction can be interesting since it just involves deuterium as fuel. This hydrogen isotope is stable and it could be obtained from the heavy water, meaning that its extraction is not so difficult. The problem associated with this reaction is the low rate coefficient and the poor released energy if compared to the other possible elements which are candidates for the nuclear fusion reaction.
The $^3He - D$ reaction is able to produce the greatest amount of energy among the other candidates. Moreover, the involved reactant elements are stable and they do not generate a neutron among the products, therefore materials activation can be avoided. Also in this case, the reaction rate for low temperatures is not high and, additionally, the ^3He can not be easily found in nature.
If a temperature around $10 - 20$ keV is considered for all the reactions, the $D - T$ one has the largest rate coefficient and the biggest cross-section: this allows to consider it as the most promising reaction. The released energy consists of $17.6MeV$ which is split between the products, $14.1MeV$ to neutrons and $3.5MeV$ to alpha particles (^4He nucleus). This means a fast neutron flux which can induce damage and activation phenomena on the components of a reactor. It must also be noticed that tritium is a radioactive isotope of the hydrogen showing a half-life of 12.33 years and it has to be produced artificially.

1.3 Plasma state

The high needed temperatures for a nuclear fusion reaction influence the state in which the fuel is found, indeed, in a such hot environment, atoms are not able to keep its electrical neutrality. Collisions between particles are so strong that hydrogen atoms are easily stripped of its electrons, resulting in a sort of gas composed by two species: ions and electrons. These two species have different charge and they are free to move, giving to the gas good conductive properties.

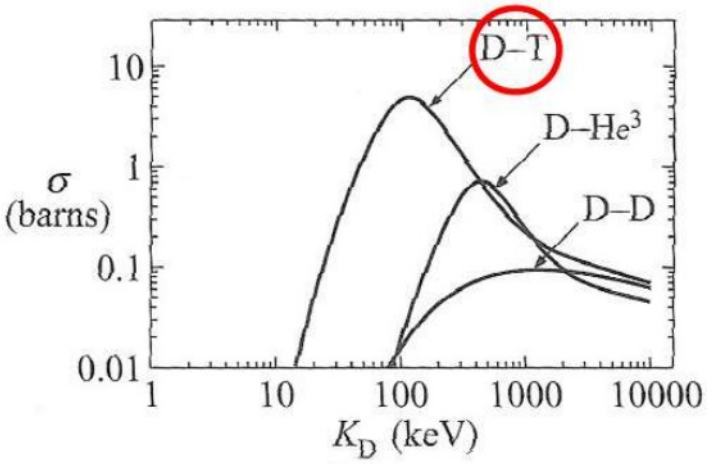

Figure 1.2: Nuclear fusion cross-section as a function of the reactants energy. The red circle indicates the peak of the cross-section for the $D - T$ reaction [2].

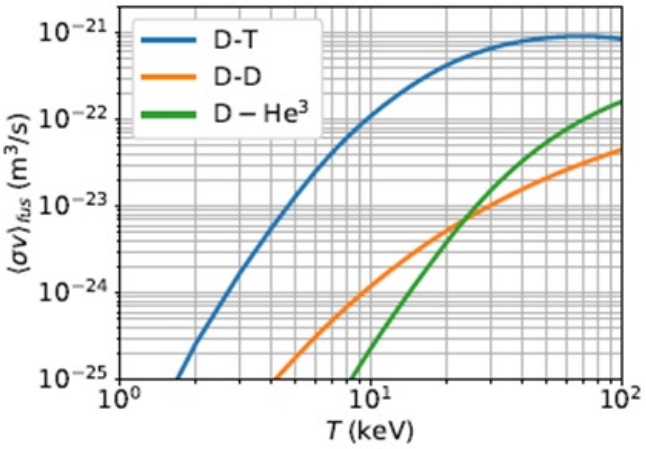

Figure 1.3: Rate coefficient $\langle \sigma v \rangle$ for different nuclear fusion reactions as a function of the temperature [3].

Moreover, ions and electrons have different masses, so electrons, whose mass is smaller, are able to more rapidly react to any external perturbations with respect to ions. When the density of this ionised gas is large, ions and electrons interact simultaneously with all the other particles composing the gas due to the long-range nature of Coulomb collisions. The interaction between distant charges will be weak, but, considering a high particles density, the cumulative effect of a large number of particles will generate a macroscopic effect. This type of effects is defined as *collective effects* and, when they are dominant, the ionised gas is called *plasma*.

Plasma is characterised by three main parameters: a characteristic length scale (called Debye lenght, λ_D), a characteristic inverse time scale (called plasma frequency, ω_P) and a characteristic collisionality parameter (the plasma parameter, Λ_D).
An ionised gas can be defined as plasma according two different criteria. One involves the macroscopic lengths and frequencies that have to be compared with λ_D and ω_P. The other is related to Coulomb collisions which determine if an ionised gas is dominated by long-range collective effects or not.
For the first criterion, the typical dimension of the ionised gas (the characteristic length L) must be much higher than the Debye length, while the macroscopic frequency, which is the inverse thermal transit time of a particle moving across plasma ($\omega_T = \frac{v_T}{L}$), has to be much smaller than the plasma frequency.
For the second, the parameter to be analysed is Λ_D, indeed, large values of this quantity are associated to low collisionality, which is required for plasma. Λ_D must be much greater than one, implying low collisionality: this means a large number of particles inside a sphere whose radius is the Debye length.
Most applications of plasma in the nuclear fusion field are related to the magnetic confinement, so fusion plasma must fulfill another constraint. When a particle is confined by a magnetic field, it rotates around a magnetic field line with a frequency, called *gyro frequency*, or *Larmor frequency* (ω_L), and a characteristic radius, called *Larmor radius* (r_L). Due to this fact, ions and electrons ω_L must be bigger than ω_T and r_L has to be smaller than L. If these two relations are satisfied, the plasma can be magnetically confined (*well magnetised plasma*) [2].

1.3.1 Ignition condition

Let us consider the $D-T$ reaction for the reasons mentioned above. There is the possibility to define a minimum temperature for fusion plasmas, that are magnetically confined, starting from the ideal ignition. This condition corresponds to a plasma steady state power balance assuming negligible heat conduction losses and no external heating, so the alpha particles power (P_α) must be of the same order of the Bremsstrahlung losses. Bremsstrahlung losses (P_β) are related to the deflection of an electron, that is approaching a plasma ion, from its trajectory, resulting in a loss of energy by radiation. This type of losses is associated with a large-deflection collision and it cannot be avoided in a plasma. The ideal ignition condition implies $P_\alpha > P_\beta$ in order to obtain a self-sustained plasma. From this equation, the ideal ignition temperature, which represents the limit that must be overcome to have any fusion yield, can be found.
In a more realistic way, the ignition condition is represented by a steady state power balance which also includes the thermal conduction losses contribution (P_k)

and the external heating (P_h).

$$P_\alpha + P_h = P_\beta + P_k \tag{1.8}$$

Since the interest is related to self-sustained fusion reactions, the external heating term can be neglected, so $P_\alpha > P_\beta + P_k$ is required. This means that, once the plasma is ignited, steady state fusion power can be generated without external power required.
The equation (1.8) can be written in terms of density, temperature and confinement time (τ_E), which is the time the plasma is maintained at a temperature above the critical ignition temperature. Proceeding in this way, the Lawson criterion can be derived and the condition for plasma ignition can be defined. Lawson criterion set the limit for the Lawson parameter, which is the product between plasma density and confinement time. By plotting $n\tau_E$ as a function of the temperature, it is possible to obtain a minimum temperature of 25 keV for the self-sustained fusion reaction involving D and T. Considering this temperature, the Lawson criterion can be written as:

$$n\tau_E \geq 2 \cdot 10^{14} \frac{s}{cm^{-3}} \tag{1.9}$$

Finally, another important term, that must be taken into account for the power balance, is the gain parameter Q. This quantity is based on physics considerations and it represents the ratio between the net output thermal power and the heating power. To obtain a net gain in terms of thermal power, the total output thermal power must be greater than the heating power needed to sustain plasma. Q can be expressed as:

$$Q = \frac{P_{out} - P_{in}}{P_{in}} \tag{1.10}$$

where P_{out} is the total output thermal power, while P_{in} is the heating power which is equal to P_h. Analysing this parameter is fundamental to understand the capability of producing energy from nuclear fusion reactions. If no fusion reactions take place, all the input heating power is converted into the total output power in the form of thermal conduction and radiation power losses: this means $P_{in} = P_{out}$ and $Q = 0$. On the other hand, if no heating power is required to sustain the reaction, so $P_{in} = 0$, Q will tend to infinity. Thus, considering a steady state power reactor, the range of the gain parameter will be $0 < Q < \infty$ [2].

1.4 Magnetic and inertial confinement

Plasma has to be confined for a certain amount of time in order to meet the Lawson criterion and reach proper conditions where the ignition of nuclear fusion reactions is achievable. In this field, there a two ways to confine plasma: the inertial

confinement and the magnetic confinement.
The first is based on the idea to create a high density plasma (in the order of 10^{23} particles per unit of volume) thanks to the action of certain lasers. These lasers have to compress and heat up a target which is filled with the fuel in form of pellets containing D and T. This process deposits energy in the outer layer of the target which, then, explodes outwards generating a shock wave able to propagate compressing and heating the D-T pellets. Powerful shock waves can generate conditions for fusion reactions. In this case, the confinement time is defined as the amount of time it takes for the energy from the reaction to be lost to the environment and it can be in the order of 10^{-9} seconds.
The second approach, instead, exploits external magnetic fields to confine plasma. Magnetic confinement aims to satisfy the Lawson criterion adopting lower density and higher confinement time with respect to the inertial case. Indeed, considering a temperature of 10 keV, typical density values are around 10^{14} particles per unit of volume, while τ_E is about 1 second. A higher confinement time is also fundamental to reach a steady state operational regime.

1.4.1 Tokamaks and Linear Plasma Devices

In the framework of this thesis, the attention will be placed on magnetic fusion devices, so the physics for the magnetic confinement adopted in several devices will be briefly described.
As anticipated in 1.3, a charged particle, subjected to an external magnetic field, rotates around magnetic field lines with a gyro frequency ω_L and a Larmor radius r_L, while moving along them. In this configuration, particles are confined in the perpendicular direction to the magnetic field, but not in the parallel one. There are two different types of device able to confine particles also in the parallel direction: open confinement systems and closed confinement systems. The difference related to these systems is found in the magnetic field lines, indeed, for the first, lines are open, starting from one side of the vessel device (the source) and ending to an other solid surface (the target). The second type shows closed magnetic field lines exploiting a toroidal symmetry.
Linear Plasma Devices (LPDs) are associated with the open confinement system, taking advantage of a specific magnetic field configuration, called *magnetic mirror*. This arrangement is based on the conservation of the magnetic moment and it characterises many experimental devices. The magnetic moment μ is defined as:

$$\mu = \frac{m v_\perp^2}{2B} \tag{1.11}$$

and it must be conserved in a fusion reactor, so $\mu = const.$ $v_\perp$ is the velocity orthogonal to the magnetic field, while the other velocity component is that one

parallel to the magnetic field lines ($v_{//}$). Since μ must be constant, an increase in the magnetic field B results in a gain of the perpendicular velocity component. Due to the conservation of energy, higher values of $v_{\perp}$ imply a decrease in $v_{//}$:

$$E = \frac{mv^2}{2} = \frac{mv_{\perp}^2}{2} + \frac{mv_{//}^2}{2} = const \tag{1.12}$$

Thus, acting on the intensity of the magnetic field, it is possible to obtain a null parallel velocity and a particle can be reflected back. This condition is reached in the *mirror point*, meaning that charged particles can also be confined in the direction parallel to magnetic field lines. Although this configuration has applications in experimental devices, it is not so effective in terms of confinement because a threshold, related to the initial component of $v_{//}$, exists. If the parallel velocity is too high, particles cannot be reflected, resulting in the failure of their confinement. This situation is valid for particles that exceed the limit of $v_{//}$, entering the so-called *loss cone*. Due to this fact, LPDs are not used to study the plasma particles confinement, but they have a fundamental role for what concerns plasma-material interaction and boundary phenomena, since they are able to reproduce particles fluxes and densities compatible with those expected in future fusion reactors.
In the framework of closed confinement systems, the most common configuration is represented by the *tokamak* which takes advantage of a toroidal symmetry. Tokamaks confine plasma particles thanks to the presence of two components of the magnetic field acting in the torus plane, the toroidal magnetic field and the poloidal one. The toroidal component of the magnetic field (B_{ϕ}) behaves like $1/R$, so, if a circular section of the tokamak is considered, it shows a decreasing trend going outwards. Plasma pressure, acting on the torus section, cannot be balanced by the single presence of B_{ϕ}, so another magnetic field component is needed: the poloidal one, B_{θ}. The toroidal magnetic field is generated by the presence of proper toroidal coils which are placed around the torus, while the poloidal component is created by the flowing of the plasma current, I_p. The existence of I_p in the toroidal chamber depends on the presence of a central solenoid located in the central part of the device. The working principle is that of a transformer: the central solenoid is crossed by a current varying in time (I_{cs}) which induces a magnetic field B_{cs}. Then, thanks to the Faraday's law, related to the variation in time of the magnetic flux of B_{cs} across the plasma magnetic axis, a toroidal electric field (E_{ϕ}) is formed. Since plasma has a finite value of resistivity, the plasma current I_p is generated due to the Ohm's law. In addition to B_{ϕ} and B_{θ}, a vertical component of the magnetic field (B_v) is also taken into account. B_v is generated by poloidal field coils situated around the toroidal ones and it has the aim to give stability to plasma in terms of shape and equilibrium. It is important to notice that the combination between B_{θ} and B_{ϕ} produces a resultant magnetic field which shows a helical path.

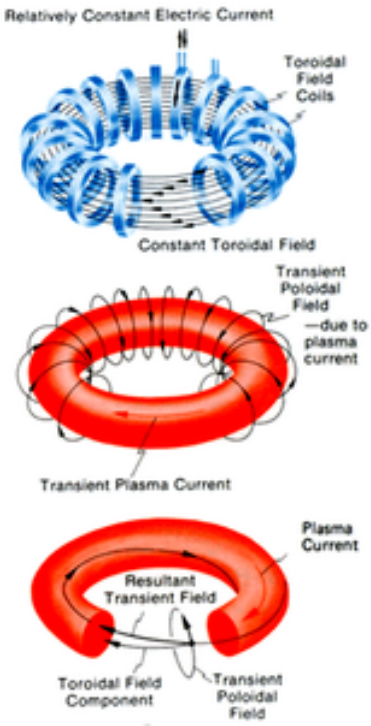

Figure 1.4: Magnetic field components in a tokamak [4].

1.5 Challenges in the nuclear fusion framework

In the nuclear fusion field, three main challenges must be considered: the power exhaust from plasma, the extraction of the power deposited by neutrons in the blanket while breeding the tritium fuel, and cooling and shielding of superconductive magnets.

- **Power exhaust**

  The power balance in a fusion reactor has to be examined and, in this case, the Ohmic heating is neglected:

  $$P_\alpha + P_n = P_{rad} + P_{cond} + P_{adv} \tag{1.13}$$

  P_α is the power carried by alpha particles, while P_n indicates that carried by neutrons. In the power exhaust framework, this last term is not relevant because plasma is completely transparent to neutrons and the power deposited will be extracted in the blanket. The other terms in the equation are related to the classical heat transfer mechanisms because plasma is a dissipative medium. P_{rad} refers to the power related to radiation, P_{cond} refers to the conduction

and P_{adv} to the advection. The advective component of the power is caused by the mass transfer, so it is linked to a macroscopic property, while the conductive term is related to microscopic transport. Both are then affected by the magnetic field because particles travel along field lines. The most important quantity in order to properly exhaust the power in a nuclear fusion reactor is represented by the heat flux and, consequently, the wetted area corresponds to the parameter of interest, since high values of this surface allow a more straightforward heat flux disposal. Radiation coming from plasma is not a problem for the power exhaust because this heat transfer mechanism is isotropic, so the wetted area can be comparable with the area of the entire first wall. Radiation can only be dangerous in the core plasma, resulting in an undesired decrease in temperature. On the other hand, conduction and advection are strongly anisotropic and this leads to a very small wetted area which has to exhaust a great amount of power. High heat loads, in the range of tens MV/m^2, are a serious problem for a reactor because they can result in damage of plasma facing components, compromising their lifetime.

- **Power extraction in the blanket and tritium breeding**

  The blanket corresponds to the first component beyond the first wall (which directly faces the plasma) and it can assume three different functions: the extraction of power deposited by neutrons thanks to the presence of a proper coolant, tritium breeding with its consequent extraction and superconductive magnets shielding.
  The so-called *Breeding Blanket* (BB) represents one of the fundamental components in a nuclear fusion reactor because it must withstand the high energy neutron flux converting the volumetric power deposition and it has to breed tritium by means of a breeder material and a neutrons multiplier. There are many proposals for a BB which foresee different types of coolant and breeder/multiplier. Tritium breeder materials are Lithium-based materials because Li is able to react with neutrons producing tritium. Two Li isotopes exist, $Li-6$ and $Li-7$, which can produce tritium according two different reactions:

$$^6Li + n \rightarrow T + {}^4He + 4.8MeV \tag{1.14}$$

$$^7Li + n \rightarrow T + {}^4He + n - 2.466MeV \tag{1.15}$$

  Most of natural lithium is constituted by $Li-7$ which can interact with a neutron resulting in tritium production only if neutrons energy is higher than a certain threshold, so the reaction is endothermic. The reaction (1.15) also generates another neutron that could again interact with Li for T production. $Li-6$, instead, gives place to an exothermic reaction. An important parameter

in this frame corresponds to the Tritium Breeding Ratio (TBR) which is the ratio between T produced in the BB and T burnt in plasma. This quantity is related to the capability of in situ fueling and it must be greater than one.
Neutrons multiplier materials have the aim to increase the number of neutrons that reach the BB. Possible choices are lithium, lead and beryllium which can be solid (pebbles) or liquid.
The coolant is selected according to the heat removal capability, the material compatibility, the temperature operating window and the possible presence of magnetohydrodynamic (MHD) effects. Actually, the considered coolants are: water, helium, liquid metals and molten salts.
The shielding function of the BB regards the vacuum vessel (VV) and the superconductive magnets (SC). For the VV, the number of displacements per atom (dpa) must be kept as small as possible, while the neutrons flux and the heat loads must be limited in order to not compromise superconductive properties for the SC.

- **Cooling and shielding of superconductive magnets**

  Superconductive magnets are the tools adopted to confine plasma in nuclear fusion reactors. Since plasma temperature is about 10^8 K and superconductors temperature must be kept around 4.5 K, reactors experience a big temperature gradient, caused also by their finite size.
  Magnets are subjected to different loads, for example: gravity loads, due to their dimensions, electromagnetic loads, due to high currents and magnetic fields, thermal loads, because superconductors thermal capacity goes quickly down decreasing the temperature, so small power deposition can result in great temperature gradients, and nuclear loads, associated to particles and radiation.
  Superconductors are constituted by a central region delimited by a spiral wire surrounded by external strands which are grouped in petals. This structure is located within a jacket conduit which is usually made of stainless steel in order to sustain high electromagnetic loads. This typology of superconductors is called *cable-in-conduit conductors* (CICC) and corresponds to the one that will be adopted for ITER applications. Setting some critical values of temperature, current density and magnetic field, it is possible to determine the superconductivity region which consists of a $3D$ space characterised by two different surfaces: the superconducting one and the normal state. The critical current density is a fundamental parameter because it allows to quantify the total current that a superconductor can carry, so magnetic field and magnets size can be obtained. Superconductors critical temperature is very low, so proper cooling is needed. The strategy adopted in this frame consists of a forced flow cooling where supercritical helium is the coolant which flows in the

superconductor central channel. Cryogenic conditions must be kept exploiting the high heat capacity of supercritical He and this can be realised thanks to the presence of a cryogenic system composed of two parts, the cryoplant and the cryodistribution. Normal operations in tokamaks are pulsed, since the current flowing in the central solenoid varies in time. his leads to pulsed heat loads that impact on magnets, so the cryogenic system must be capable of facing a transient behavior.

Chapter 2

SOL and edge plasma physics

The topic of this thesis is placed in the context of exhausting the power coming from plasma, so plasma boundary phenomena must be shown. In this chapter, the physics regarding SOL and plasma edge will be offered in order to introduce the plasma-surface interaction and Plasma Facing Materials (PFM).

2.1 Divertor and limiter configurations

In the context of magnetic confinement in tokamaks, the magnetic field configuration is designed to encompass a three-dimensional space, comprising nested and toroidal magnetic surfaces. Within the main plasma region, these magnetic surfaces are enclosed. However, as they extend outward, they encounter the first wall, resulting in particle-wall collisions. Consequently, the plasma is effectively segregated into two distinct regions: the core plasma and the region characterized by open magnetic surfaces. The first is related to closed magnetic surfaces, while the latter extends beyond the *Last Closed Magnetic Flux Surfaces* (LCFS) radially for a few centimeters generating what is known as the *Scrape-Off Layer* (SOL). The SOL, a thin plasma region, is delimited from the core plasma by the separatrix, marking the boundary between the two plasma regions. Although closely linked, it is worth noting that the edge plasma slightly differs from the SOL as it also includes a small portion of plasma inboard of the LCFS.
Two primary options are employed for generating a separatrix: the limiter configuration and the divertor configuration.
The limiter mechanically delimits the core plasma and SOL region creating a separatrix thanks to a tangency point, where the distance between the core plasma and the solid surface is null. Accordingly, this configuration can lead to a quick

contamination of impurities from the wall inside the core plasma.
Over the years, various limiter layouts have been proposed. The initial option involved the rail-limiter configuration, distinguished by a single contact point. Subsequently, a poloidal limiter, consisting of two half rings, was introduced to provide increased flexibility. Although this configuration was movable, it had a restricted wetted area (A_{wetted}, i.e. the contact region between plasma and solid surfaces). As a result, another limiter type, the toroidal limiter, was implemented. While it offered a larger A_{wetted}, it was stationary, leading to a decrease in flexibility.
The divertor configuration, on the other hand, aims to create a separatrix in a magnetic way exploiting proper magnets which can generate a poloidal magnetic field able to superimpose to the one of the tokamak. In this case, a contact point between core plasma and SOL, called X-point, develops. Here, the poloidal component of the magnetic field cancels out. The magnetic field line traversing this point corresponds to the separatrix, which partitions the plasma into the core and SOL regions. With this configuration, another region emerges known as the *private plasma*, situated between the two separatrix legs and terminating at the divertor targets.
The most common divertor configuration is the *Lower Single Null* (LSN): a divertor coil, placed in the lower part of the reactor, creates a current which has the same direction as the plasma current (counterclockwise). Both generate a poloidal component of the magnetic field that vanishes in the X-point, the location where the two components of B_θ encounter. In this way, it is possible to divert the magnetic field lines, outside the separatrix, which end in the divertor plates. The point where the separatrix impacts on the divertor target is called *strike point*.
Thanks to the divertor configuration, surfaces associated with the source of impurities, such as the divertor targets, are moved away from the main plasma, so core contamination is avoided, and the nuclear fusion fuel in this region is not polluted. Impurities cannot flow upstream against the direction of the magnetic field lines, and at the same time, they can serve a beneficial role in dissipating power in the plasma edge through radiation. This is an isotropic and volumetric process able to spread power coming from plasma particles on a larger area guarantying a bigger A_{wetted}. Radiation exploits impurities arising from divertor targets and those related to impurities seeding, which consists of the injection of neutral gases in the SOL region.
Finally, the divertor configuration also allows to have a constant sink which is represented by the pumping of plasma that is not burnt. This type of pumping mechanism is not feasible in a limiter configuration due to the constrained space available.

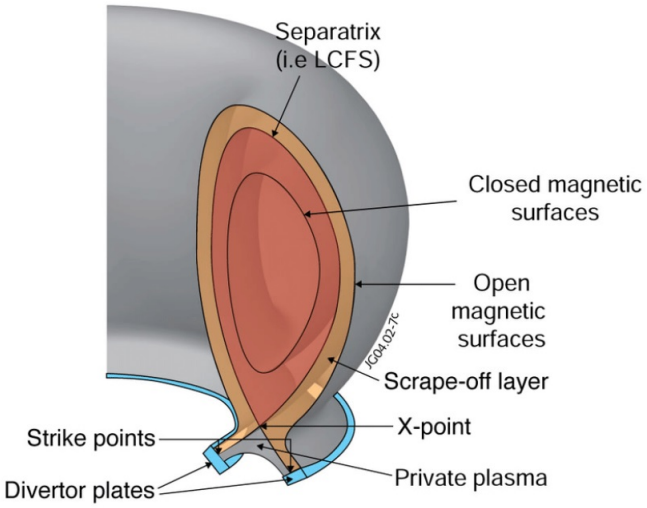

Figure 2.1: The divertor configuration of a tokamak [5].

2.2 Electrostatic sheath

Particles can cross the separatrix due to radial transport mechanisms, like collisional diffusion, plasma turbulent transport phenomena and drifts. In this region, free streaming along the magnetic field and radial transport must be considered. Ions and electrons follow the magnetic field lines reaching the wall at an equal rate, hence a net electric charge cannot be created.
When plasma particles hit the walls, the recycling phenomenon occurs: ions and electrons recombine at the wall generating neutral atoms (or molecules) which are, then, released towards the main plasma. In this case, the wall corresponds to a perfect sink, since the overall mass balance is not perturbed, and all particles are re-emitted. Thus, the plasma motion in the SOL region is affected by the pressure gradient determined by the walls and plasma particles are accelerated following the magnetic field lines.
To analyse the SOL region, calculating the collisional mean free path is essential. However, by looking at this region from a macroscopic point of view, it can be effectively characterised by a fluid model. In this model, the primary drivers are sources, which are associated with ionisation processes and particles feeding, and sinks, which represent particles leaving the SOL in proximity of the wall.
Plasma is typically characterised by quasi-neutrality ($n_e = n_i$) for distances larger than the Debye length. Nevertheless, this assumption does not hold when plasma is in close proximity to the wall. Consequently, a kinetic treatment can be adopted. The particles current hitting the wall is represented by a half-Maxwellian flux,

where the velocity depends on the temperature and the particle mass.

$$\Gamma_{wall} = \frac{1}{4} n_{wall} \bar{c} \tag{2.1}$$

$$\bar{c} = \sqrt{\frac{8T}{\pi m}} \tag{2.2}$$

Where $\bar{c}$ is the average velocity and n_{wall} is the particles density approaching the wall.
Since ion and electron temperatures are approximately equal, the flux of electrons directed towards the wall would exceed that of the ions due to their mass difference. In this way, the plasma would build up an electric charge, so the following processes can be taken into account until the steady state is reached.

- Electrons start to accumulate creating a negative charged layer in front of the wall.
- The increasing electric field begins to repel electrons while simultaneously attracting ions, until the steady state condition is reached, i.e. $\Gamma_e = \Gamma_i$ at the wall.
- At the steady-state, ions distribution will be strongly perturbed, while electrons distribution is still fully Maxwellian.

For the sake of simplifying the analysis, ion temperature will be assumed to be zero, so ions distribution can be considered as a monocromatic beam with a narrow trend in the velocity space. In this way, an electrostatic sheath is generated for distances comparable with the Debye length resulting in a mismatch between ion and electron density. In this region, quasi-neutrality does not hold, and the electric potential can be calculated thanks to the Poisson equation.

$$\frac{d^2\Phi}{dx^2} = \frac{e}{\epsilon_0}(n_e - n_i) \tag{2.3}$$

Ion density can be calculated thanks to the energy conservation inside the sheath edge.

$$\frac{m v_{se}^2}{2} + e\Phi_{se} = \frac{m v^2}{2} + e\Phi \tag{2.4}$$

$$n_{se} v_{se} = n_i v \tag{2.5}$$

$$n_i = \frac{n_{se}}{\sqrt{1 + \frac{2e}{m v_{se}^2}(\Phi_{se} - \Phi)}} \tag{2.6}$$

Electron density is calculated from the electron momentum equation, adopting the Boltzmann equation.

$$n_e = n_{se} e^{-\frac{e}{T_e}(\Phi_{se} - \Phi)} \tag{2.7}$$

Substituting in (2.3) and manipulating the terms, it is possible to derive:

$$\frac{d^2(\Phi - \Phi_{se})}{dx^2} = \frac{e^2 n_{se}}{\epsilon_0}(\frac{1}{T_e} - \frac{1}{m v_{se}^2})(\Phi - \Phi_{se}) \tag{2.8}$$

In order to obtain physical results, potential oscillations must be avoided, and it is valid for:

$$\frac{1}{T_e} - \frac{1}{m v_{se}^2} \geq 0 \tag{2.9}$$

and so,

$$v_{se} \geq \sqrt{\frac{T_e}{m}} \tag{2.10}$$

Assuming T_i null, this equation becomes:

$$v_{se} \geq c_s \tag{2.11}$$

Where c_s is the speed sound and the subscript *se* refers to the sheath edge.
In the main SOL plasma velocity cannot exceed the sound speed, while at the entrance of the sheath (2.11) applies, thus, to satisfy both the requirements:

$$v_{se} = c_s \tag{2.12}$$

This result is known as *Bohm criterion*.
The potential drop associated with the electrostatic sheath is about three times the electron temperature ($\simeq 3T_e$). Thus, an ion crossing the sheath acquires an energy equal to this quantity, while an electron loses the same amount of energy. Consequently, the total power leaving the plasma at the sheath is the same that reaches the wall, but its distribution between ions and electrons is different. Therefore, an ion impacting the wall carries the majority of the power and possesses a greater likelihood of causing damage compared to an electron, partly due to its higher momentum.

2.3 The sputtering phenomenon

Sputtering is a critical phenomenon responsible for damaging the wall and is a primary concern regarding the lifetime of components directly exposed to plasma. It involves the ejection of atoms from a solid surface when they receive a sufficient amount of energy to overcome the surface binding energy.

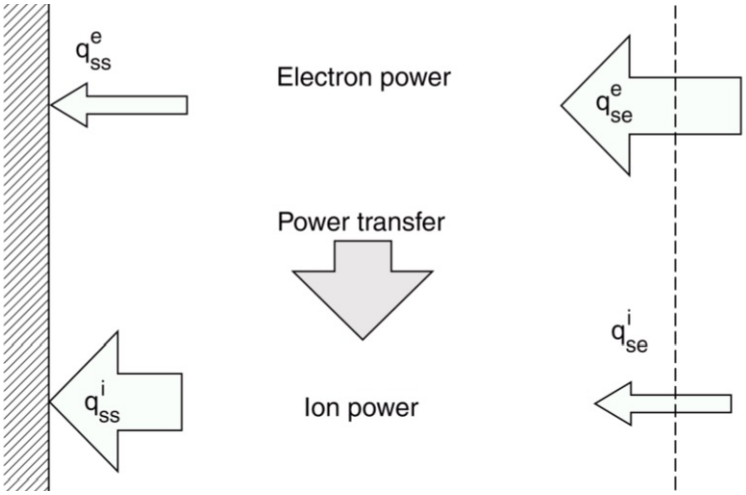

Figure 2.2: Different distribution of the power between ions and electrons [6].

Energetic ions are accelerated due to the presence of the electrostatic sheath in front of the solid wall, and they collide with it resulting in a momentum transfer to atoms in the solid lattice. This process is controlled by the pair ion-element wall composition and by the electron temperature due to the sheath power transfer. In this context, it is important to make a distinction between physical sputtering, related to the atom removal caused by momentum transfer, and the chemical sputtering, which foresees the formation of molecules due to chemical reactions between solid surface atoms and incident particles.
Referring to the first case, the physical sputtering yield serves as a fundamental measure, providing an estimate of the number of wall atoms removed by a single incident ion. This quantity depends on the energy of the projectile ion, rising until it reaches a maximum, which corresponds to a certain energy, after which it decreases monotonically. This means that at ion energies larger than the one in correspondence of the maximum, the process involves atoms which are deeper inside the surface, reducing the impurity production. Moreover, the sputtering yield increases with the mass of the impinging ion and diminishes with the mass of the target atom.

2.4 SOL width and power reaching the target

Another crucial aspect to analyse is related to the width of the SOL. This concept is not simple, and a general formula is not available, but several distinctions can be made.
Firstly, SOL width can be estimated on the presence of particles at a certain

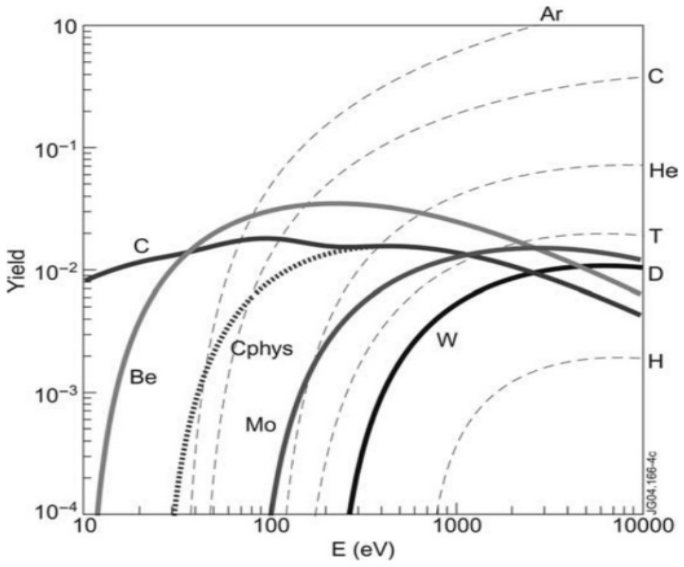

Figure 2.3: Physical sputtering yield for selected projectile-target couples as a function of the projectile energy [7].

distance from the separatrix, leading to a value called λ_n. Another value for this parameter can be determined considering the SOL as the region where particle temperature is still relevant, and this is related to λ_T. Finally, SOL width can also be referred to as λ_q, and it regards the presence of a great power flux parallel to the magnetic field lines. These different values of SOL width are useful to determine the parallel component of the heat flux, so that component transported along the magnetic field lines. This quantity is fundamental because it allows to find the wetted area for the power exhaust. The parallel heat flux can be simplified as the product between the particle flux and the energy that, for a thermo-nuclear plasma, can be approximated with the temperature. Temperature has an exponential decreasing trend in the SOL, starting from the midplane till the divertor wall, and λ_T is the characteristic length. Considering the divertor wall with a certain inclination and λ_q as a harmonic combination of λ_T e λ_n, the so-called *Cosine model* can be defined:

$$q_{//} = q_0 e^{-\frac{y}{\lambda_q}} cos(B, \hat{n}) \tag{2.13}$$

Where q_0 is a normalisation constant, the y coordinate represents the radial direction and $cos(B, \hat{n})$ is the projection of the parallel heat flux on the surface, whose normal is $\hat{n}$.
This model takes care of the wall inclination thanks to the scalar product of the poloidal component of the magnetic field and the normal to the wall. In this way, the parallel heat flux can be plotted as a function of the poloidal angle and the

total power deposited can be found by integrating all over the surface. The value of interest of $q_{//}$ is its peak which can be slightly increased due to the plasma radiative power that reaches the divertor wall and due to the perpendicular component (to the magnetic field lines) of the heat flux.
It is fundamental to notice that the power leaving the core in proximity of the outer midplane is split in two fractions, so 50% of the power is directed to the divertor target and the other 50% goes upwards. By referring to the parallel heat flux, an upstream $q_{//}$ and a target $q_{//}$ can be considered. The first one is much higher than the latter because the power leaving the core plasma crosses a smaller area:

$$Area = 2\pi R_u \lambda_q (\frac{B_\theta}{B})_u \tag{2.14}$$

Where R_u is the upstream plasma radius.
Thanks to the magnetic flux expansion, so the ratio between the poloidal component of the upstream magnetic field and the target one, and to the target tilting, so the inclination of the divertor target in the poloidal plane (β is the tilting angle), the area crossed by the plasma power is increased, leading to a lower value of parallel heat flux.

$$Area = \frac{2\pi R_t \lambda_q (\frac{B_\theta}{B})_u}{sin\beta (\frac{B_\theta}{B})_t} \tag{2.15}$$

R_t is the plasma radius at the target location.

2.5 The 2-Point Model

In order to understand the difference between upstream plasma parameters and those at the target, the 2-Point Model must be introduced.
In this model, the SOL is considered as a long magnetic flux tube which connects the main plasma (the upstream region) to the target. The contact region between the core plasma and the SOL, despite it is quite extended, is assumed to have collapsed at a single point. Furthermore, no energy losses are supposed along this flux tube, hence all the energy entering the SOL upstream flows down to the target. Additionally, particles coming from the recycling phenomenon ionise very close to the emitting wall due to the presence of an ionisation region for electronic temperatures lower than 10 eV. These particles dominate the global particles balance, so possible sources located upstream are negligible. Due to this assumption, the flow velocity along the SOL can be considered as zero except for a thin layer between the ionisation region and the target wall, where the flow velocity reaches the sound speed. No momentum losses are also assumed, resulting in a constant total pressure along the SOL region.

$$p_{tot} = const = 2nT + nmv^2 \tag{2.16}$$

$$2n_tT_t + nmv_t^2 = 2n_uT_u \tag{2.17}$$

These equations show the pressure conservation along the SOL considering a null upstream velocity. The subscript t refers to the target, while u is related to the quantities upstream.
Substituting the velocity at the target with the sound speed, the following relations are written:

$$v_t = c_s = \sqrt{\frac{T_t}{m}} \tag{2.18}$$

$$2n_tT_t = n_uT_u \tag{2.19}$$

Since the velocity is practically zero in most of the SOL, kinetic energy of the flow and convection are neglected, thus the energy flux is purely conductive.

$$q_e + q_i = \chi_e \frac{\partial T}{\partial x} + \chi_i \frac{\partial T}{\partial x} \tag{2.20}$$

With $\chi = k_0 T^{5/2}$.
The heat flux is carried by electrons and ions, but they show a different conductivity. Specifically, k_{0e} is greater than k_{0i}, resulting in a predominance of the electrons heat flux for most of the SOL.

$$q_e = k_{0e} T_e^{5/2} \frac{\partial T}{\partial x} \tag{2.21}$$

At the target, ions and electrons energy fluxes must be summed up, leading to a heat flux term parallel to the magnetic field lines, $q_{//,t}$.

$$q_{//,t} = \gamma n_t T_t c_s \tag{2.22}$$

Where γ is an experimental parameter usually equal to 7.
Thanks to the 2-Point Model two important relationships can be derived:

$$T_t \propto \frac{1}{n_u^2} \tag{2.23}$$

$$n_t \propto n_u^3 \tag{2.24}$$

Therefore, the temperature near the target rapidly decreases with n_u, and n_t is also extremely sensitive to n_u, leading to a significant dependency of the particle flux at the target on the density upstream.
According to this model, two different SOL regimes can be detected: the sheath limited regime and the conduction limited regime.
The former scenario exhibits a constant temperature along the SOL for high values of parallel heat flux. This phenomenon arises from an increase in the electron

conductivity χ_e, which depends on the temperature. Consequently, there is the possibility to accommodate extremely large heat fluxes with moderate temperature gradients.
Conversely, the latter situation is associated with lower values of parallel heat flux, wherein the heat conductivity fails to flatten the temperature profile and strong gradients can develop. In this regime, the target temperature is much smaller than the upstream one.
Finally, the sheath limited regime is characterised by low collisionality, while the conduction limited regime shows a high collisional plasma. The conduction limited regime is also called *high recycling regime* because low values of T_t are also obtained with high n_u, that means great particles flux ($\Gamma_t = n_t c_s$) hitting the target and recycled back into the SOL. Γ_t is not directly associated with the particle flux leaving the core plasma region, indeed the particles balance mainly takes place in the region close to the target, where recycling and ionisation occur.
The last important contribution to the parallel heat flux reaching the wall is represented by the ionisation of neutral particles. The following relation can be written:

$$q_{//,t} = \gamma n_t T_t c_s + n_t c_s \epsilon_{ion} \tag{2.25}$$

Where ϵ_{ion} is the fraction of neutral particles which are ionised.
Considering no friction along the SOL, pressure is equal to the product between particles density and temperature, so:

$$q_{//,t} = \frac{p_u}{\sqrt{m}}(\gamma\sqrt{T} + \frac{\epsilon_{ion}}{\sqrt{T}}) \tag{2.26}$$

Where p_u is the upstream pressure.
This relation shows that there can be a high values of heat flux, if the temperature decreases, due to the constant pressure. Thus, friction inside the SOL region is needed in order to reduce $q_{//,t}$. Both plasma and heat flux must be lowered to obtain the so-called detachment.

2.6 Detachment

According to the 2-Point Model, the particle flux at the target is given by (2.24). Experimental evidence has shown that increasing the plasma density upstream leads to a decrease in divertor target temperature and density, consequently reducing the particle target flux. This plasma characteristic, which contradicts the physics analysed in the 2-Point Model, defines a new operational regime referred to as *detachment* (or divertor detachment).
This phenomenon is linked to significant gradients in plasma pressure parallel to magnetic field lines, resulting in a reduction of the plasma power directed towards

the divertor targets. Thus, the detachment is able to decrease the heat load on plasma facing components, the target temperature and the particles flux, while limiting the sputtering at the same time.
To create a physical model for the detachment, some friction factors related to the losses along the SOL must be introduced. These are associated with the loss of momentum, which affects the target pressure, and loss of power, which corresponds to the reduction of the parallel heat flux reaching the target. By introducing these factors in the 2-Point Model, the following relations can be written:

$$(1 - f_{power})q_{//,t} = \gamma n_t T_t c_s \tag{2.27}$$

$$p_t = \frac{1}{2} f_{mom} p_u \tag{2.28}$$

And, after some terms manipulation:

$$\Gamma_t \propto \frac{f_{mom}^2}{1 - f_{power}} \tag{2.29}$$

These relations show that both momentum and power losses acting together are needed. Indeed, if only momentum losses are considered the drop in the particle flux is related to (2.29), but the power reaching the target is not reduced since the power losses term in (2.27) is null. On the other hand, if only power losses are present, $q_{//,t}$ decreases, but there is no influence in the target pressure equation and Γ_t can increase, according to (2.29).
Divertor detachment is desirable in a nuclear fusion reactor, so understanding and controlling this phenomenon is fundamental to reduce the power load to plasma facing components. Lastly, detachment occurs at low temperatures, thus atomic and molecular processes in the SOL region must be studied.

2.7 Other models to study the SOL

The 2-Point Model is one of the simplest approaches to study the processes that occur in the SOL. It is a zero dimensional model which can provide information at just two points along this region, the target and the upstream point. Therefore, more complex models can be derived in order to study all the phenomena affecting the SOL. Among these patterns, it is possible to identify one dimensional models, like the 1D, along-B model and the *Onion-Skin Method* (OSM), but two and three dimensional approaches are also present.
The 1D, along B model can study the density, the electron and ion temperature, the parallel velocity and the parallel energy transport by exploiting laws of conservation of energy, particles and momentum. All the previous quantities are considered as a function of the distance along the SOL and of the magnetic field, and, in this way,

are not related to only two points. This type of model cannot give information about the cross-field variations of plasma quantities, so other methods are necessary. Cross-field variations of plasma in the SOL region are the strongest ones, so a more sophisticated 1D approach is needed. In this case, the OSM can be applied. This model aims to separate the entire SOL in several flux tubes which are nested inside each other and treated by means of 1D, along-B modelling. Thanks to this method, a 2D solution can be obtained by analysing the parallel and cross-field balances sequentially and iteratively. In this model, cross-field transport coefficients are treated as outputs.
In order to have a complete 2D analysis of the SOL, standard 2D edge fluid codes, like SOLPS-ITER, must be employed. These codes adopt 2D conservation equations and apply upstream boundary conditions by using the density on the last closed magnetic flux surface and the power entering the SOL. Transports coefficients are considered as an input and the parallel and cross-field balances are solved in a simultaneous way. Thus, two directions can be identified: the radial direction, related to the cross-field variations, and the one along the magnetic field. For tokamak cases, the toroidal simmetry is imposed, but, when this characteristic is not present, a 3D treatment is required [8].

2.8 Plasma-neutral interactions and radiative processes in the SOL region

The investigation of atomic and molecular species existing within the edge plasma is crucial for comprehending significant phenomena associated with the SOL region. The presence of neutral particles in the SOL, where temperatures are much lower with respect to the core plasma region, can be caused by the external gas puffing, which has the aim to refuel plasma, and by the recycling process. This last phenomenon consists of the interaction between plasma particles and reactor walls. Thus, ions impinging on a solid surface can be backscattered again in the SOL or recombine with electrons from the wall and thermalise nearby the surface. The starting point of the recycling process is represented by a perfectly clean state wherein the solid wall is full of sites where plasma ions can be absorbed and then recombine with electrons. This mechanism lasts until the wall becomes saturated: particles, that have recombined, are not anymore able to diffuse in the bulk of the wall material, so neutral particles are released. A steady state situation, resulting in the flux equilibrium, is reached. Neutral particles quickly ionise in front of the wall flowing again towards the solid surface due to the action of the magnetic field. This stationary recycling regime implies a plasma constant density if a pumping system mechanism is not present, leading to the absence of external re-fueling. It must be said that, in a real fusion reactor, an active pumping mechanism is

necessary to remove the helium ash, so this system and the gas puffing one are always present.
Plasma particles can interact with neutral atoms and molecules resulting in different processes. It is worth noting that in these example an hydrogenic plasma is taken into account.
One of the key interactions involving a hydrogen atom and a hydrogen ion (a plasma proton) is the charge-exchange mechanism. This process occurs at the low temperatures present in the SOL and it leads to the biggest exchange of momentum. A cold hydrogen atom collides with a hot plasma proton resulting in an exchange of the charge. The parent hydrogen atom turns into a cold proton leading to a loss of momentum for the plasma due to the proton reduced speed. Conversely, the parent plasma proton becomes a hot hydrogen atom, which is faster. This neutral particle is not confined by the magnetic field and can damage the solid wall inducing sputtering.

$$H^+(hot) + H^0(cold) \rightarrow H^0(hot) + H^+(cold) \tag{2.30}$$

Furthermore, the elastic collision between a neutral particle and a charged one from plasma is a similar process which does not foresee a change of the charge of the particles joining the interaction.
Electron impact ionisation is another important process which foresees the interaction between an electron and a neutral particle. A hot plasma electron collides with a hydrogen atom releasing an atomic electron. After the interaction, the impacting electron is colder, while the hydrogen ion is affected by the magnetic field and can damage the solid wall.

$$e^- + H^0 \rightarrow H^+ + 2e^- \tag{2.31}$$

Before plasma particles hit a solid surface, the recombination phenomenon can also occur. This mechanism is characterised by the interaction between an electron and an ion in the region in front of the wall. The result consists of a neutral hydrogen atom and a loss of energy for plasma.

$$e^- + H^+ \rightarrow H^0 \tag{2.32}$$

The presence of impurities and neutrals particles in the SOL region can also lead to two other processes in which radiation is foreseen. These are the Bremsstrahlung radiation and the line radiation mechanisms.
Bremsstrahlung radiation corresponds to the deflection of a plasma electron which is approaching an ion. The electron trajectory is perturbed by the presence of a charged particle, so the e^- is slowed down, losing a certain quantity of energy, and a photon is emitted due to the conservation of energy. This type of energy loss cannot be avoided and it is proportional to the impact parameter, so the distance between the electron trajectory and the ion, the electron velocity and the

ion atomic number. Specifically, Bremsstrahlung radiation is linked to the quantity Z_{eff}, which indicates the overall impurity contamination of plasma.

$$Z_{eff} = \frac{\sum_{j=1}^{N} Z_j^2 n_j}{n_e} \tag{2.33}$$

The last radiative process is represented by line radiation. An electron from the plasma collides with an atom or ion, causing excitation, which results in the transition of an atomic electron to a higher energy level. Subsequently, a photon is emitted as the electron returns to its original energy level. This mechanism is able to very effectively cool down plasma in the SOL region. However, if an atom has a high atomic number, it is never fully stripped of its e^-, so the core plasma region can also be cooled, resulting in the nuclear fusion reaction contamination.
The radiative power is proportional to the radiation function L_z. This quantity varies depending on the type of impurities/neutral particle inside the plasma. Thus, it relies upon the atomic number Z, the electron temperature and the impurity residence time. L_z includes both the contributions of Bremsstrahlung and line radiation, and it increases when the electron temperature grows. When considering a low Z impurity responsible of radiation, it is important to note that the contribution of line radiation in L_z ceases to exist at high T_e because the atom is fully ionised.

2.9 Plasma facing materials

Plasma facing materials (PFM) are those materials that constitute components directly exposed to the plasma in a nuclear fusion device. These materials must protect inner components from particle flux and, at the same time, they have to deal with a very harsh environment, since they must withstand high thermal loads and temperatures.
The proper choice of PFM is not straightforward because materials have to be selected according to certain characteristics, which include high thermal conductivity, high melting point, low erosion (related to plasma particles bombardment), low activation by neutrons and compatibility with plasma hydrogen isotopes. An important restriction for PFM is associated with the atomic number Z, which allows for the distinction between high Z materials and low Z materials. High Z materials can effectively minimise erosion, as the particle energy flux is lower than the binding energy of the molecules. On the other hand, low Z materials can be adopted to decrease plasma cooling and facilitate neutron scattering, thereby enhancing energy conversion.
The radiative cooling of the plasma is proportional to the material atomic number. Therefore, low Z materials tend to have low cohesive energy being more susceptible

to the sputtering phenomenon.
The requirement of both low Z and high Z materials for plasma facing components can seem contradictory, but it is a fundamental challenge that has to be met for future nuclear fusion reactors. High Z materials are characterised by low erosion, but, when an atom is sputtered from a solid wall, it can be dangerous in term of plasma cooling because it is not fully stripped of its electrons, so it can radiate by means of line radiation. This phenomenon can cool plasma in the SOL region, but also in the core region where high temperature nuclear fusion reactions take place. The choice of the proper material is very challenging and some changes have been made over the years. In the ITER divertor case, for instance, the material initially selected for this component was carbon. Specifically, a carbon-carbon composite material was chosen, comprising a carbon matrix reinforced with carbon fibers (CFC). This material shows good thermal shock and thermal fatigue resistance, high thermal conductivity, absence of a melting point and a low radiative power loss due to low Z. Nevertheless, CFC has been discarded because of its high tritium retention. Carbon undergoes to chemical sputtering and, after the interaction with the hydrogen plasma, it can produce layers of hydrogenated carbon films which are able to retain tritium due to the presence of hydrogen isotopes.
The actual configuration of the ITER divertor foresees tungsten as PFM. Tungsten is characterised by high melting point, low erosion, high thermal conductivity, high thermal stress resistance and low tritium retention. However, problems related to this element are associated with its high atomic number (Z=74) which means that very low tungsten concentrations are allowed in the plasma due to its capability to radiate thanks to the line radiation mechanism.
Within the context of materials for the divertor, it is fundamental to mention the possibility of using liquid metals in order to take advantage of the vaporisation latent heat to exhaust high heat loads. Features of a liquid metal divertor will be described in the next chapter.

Chapter 3

The Liquid Metal Divertor

ITER divertor, as previously mentioned, will be composed of actively cooled tungsten monoblocks. Then, to reduce the heat load reaching this component, a proper impurity seeding is foreseen in order to obtain plasma detachment and radiation in the SOL region. Adopting a solid divertor configuration can lead to plasma facing component damages which include cracking, erosion, melting (if the heat flux overcomes the critical heat flux) and fatigue failure.
These problems are crucial, especially if the EU-DEMO case is considered, indeed, larger unmitigated parallel heat fluxes and a bigger amount of stored energy in the core plasma are expected. These harsh operating conditions require that other solutions are investigated. One of the most promising layouts in this field corresponds to the Liquid Metal Divertor (LMD) configuration.

3.1 LMD general features

LMDs represent a viable alternative to solid divertors, as they can avoid cracking phenomena and mechanical failure, while showing a greater heat handling capability. Furthermore, this technology allows to design a thinner component with respect to a solid divertor due to the possibility of resupply eroded regions with new molten materials, leading to an elimination of lifetime issues.
Most of the problems related to this configuration is found in the erosion. LMDs show a higher erosion rate which means a bigger plasma contamination with respect to a solid divertor. Consequently, a system of collection and recirculation for the liquid metal is needed.
LMDs are able to remove power through different channels since they can take advantage of the evaporative cooling and the presence of intrinsic impurities, which generate the vapor shielding phenomenon. Vapor shielding consists of the interaction between plasma particles and evaporated liquid metal particles. The

first, hotter and more energetic, collide with the vapor which can radiate energy by means of ionisation, line radiation and Bremsstrahlung. This phenomenon is able to reduce the heat fluxes approaching the divertor, although part of the energy is also radiated towards this component. Vapor shielding has also an important role in terms of liquid metal mass balance: plasma particles ionise metal particles which resent the magnetic field lines being transported towards the divertor target where they re-deposit. This effect is known as *entrainment effect*. Vapor shielding phenomenon can also be fundamental in the off-normal transient case resulting in a reduction of the heat load on the divertor surface and in an effective shielding.
LMDs also exhaust heat by means of heat conduction, due to the high thermal conductivity of the liquid metal, and also by an additional impurity seeding. Other advantages are related to the capability of self-healing, a non-net erosion, due to the possibility of replenishment, and higher resistance to neutron damage, because a neutron loading cannot generate defects in liquid.
Like a solid divertor, LMDs show erosion processes due to the heat and particles load impinging on the target, resulting in the need of a constant replenishment of liquid metal. All the erosion mechanisms are listed below [3].

- **Physical sputtering**
  This phenomenon is related to the transfer of momentum caused by energetic ions (or neutral atoms) which hit wall atoms (see section 2.3). It is a threshold process, indeed the sputtering yield shows a lower bound for the projectile ions energy. This threshold is small for low Z materials and bigger for high Z materials.

- **Evaporation/condensation**
  This process is extremely relevant for liquid metals and liquid plasma facing surfaces in general. The evaporation increases following the surface temperature trend and it is not dependent on the particle flux hitting the divertor.

- **Thermal sputtering**
  Experimental evidence indicates that, in certain materials, the sputtering yield is also influenced by temperature. In this case, energetic particles impinging on a liquid surface can create *adatoms* which are freely bound to the surface, resulting in an evaporation that occurs at lower temperature.

Moreover, erosion mechanisms can be reduced by redeposition processes which aim to lower the erosion rate. Erosion suppression mechanisms are:

- **Prompt redeposition**
  It is caused by the ionisation of eroded neutral atoms within one gyro-radius from the divertor surface (*magnetic pre-sheat*). This results in the returning of particles to the surface.

- **Non-prompt redeposition**
  This process is similar to the one mentioned above, but it foresees the particles ionisation also in a region outside the pre-sheath one. These particles can be redeposited on the surface due to the action of friction and thermal processes.

- **D retention effect**
  It can be an erosion suppression mechanism, but it depends on the choice of the liquid metal and its retention capability.

Finally, employing an electrically conductive liquid metal in the presence of strong magnetic and electric fields can induce magnetohydrodynamic (MHD) forces capable of destabilising the liquid surface, thereby causing instabilities and droplet formation, which may increase the erosion.

3.2 Liquid metal choice

Selecting the appropriate liquid metal is not a straightforward decision, and extensive testing over the years has highlighted two promising candidates: lithium (Li) and tin (Sn). Both metals exhibit a low melting point, making them favorable options.
Lithium is characterised by a high vapour pressure which means a high evaporation rate for temperature higher than $600°C$. This suggest a significant presence of Li in the SOL region, which is beneficial for the vapor shielding phenomenon. However, an excessive amount of lithium atoms can dilute the fuel causing a substantial plasma contamination. This element shows a low atomic number (Z=3), which means it does not represent a danger in terms of core plasma cooling, as its contribution to line radiation and Bremsstrahlung in the radiation function is low. This is because lithium is easily stripped of its electrons and has a poor Z_{eff}. Lithium reacts with hydrogen at temperatures higher than $500°C$. Additionally, there could be safety risks in the event of a water leak, as lithium undergoes an exothermic reaction with H_2O. Finally, Liquid Li has also some issues related to the tritium retention, due to the high affinity of lithium for H-isotopes. Nevertheless, it has been demonstrated that this phenomenon become negligible at temperatures greater than 650 K.
Tin exhibits a low vapor pressure and consequently a lower evaporation rate compared to lithium. This leads to a more moderate presence of tin vapor in the SOL region and a broader temperature range in which it remains in vapor form. Sn has a higher radiative function and it is able to radiate more in the core plasma due to its atomic number (Z=50), resulting in an excessive cooling in the region where the fusion reaction takes place. Moreover, liquid tin does not have problems related to the tritium retention, although this characteristic has to be confirmed by future

studies. However, it entails technological challenges associated with the corrosion during the liquid metal flowing.

Quantity	Unit	Meaning	Li	Sn
Z		Charge	3	50
A	amu	Mass number	6.94	118.7
T_m	$°C$	Melting temperature	180.5	231.9
ρ	kg/m^3	Density at T_m	512	6990
T_b	$°C$	Boiling temperature	1347	2270
Δh_{evap}	$\cdot 10^6 kJ/kg$	Latent heat of evaporation	1.02	35.15
k	$W/(mK)$	Thermal conductivity at T_m	45	30

3.3 LMD configurations and design

Three main LMD concepts can be considered: the flowing LMD configuration, the vapour box configuration and the ITER-like liquid metal divertor which foresees the use of a capillary porous structure (CPS).
Flowing LMDs are based on ThermoElectric MagnetoHydroDynamic (TEMHD) effects which can passively promote a radial flow of liquid metal. Thanks to the presence of thin trenches, the liquid metal can be confined by the surface tension, while its flow is promoted by the combination between a thermo-electric current and the magnetic field. This configuration is able to exhaust the heat flux coming from plasma and, at the same time, to continuosly provide a liquid metal flow to the plasma facing surface of the divertor. One example of flowing LMD consists of the Lithium Metal Infused Trenches (LiMIT) design which allows to reach the low recycling regime for tokamak operations thanks to the high rate of surface renewal combined with the Li capability to retain hydrogen. This technology produces a liquid metal flow driven by and proportional to the plasma heat flux which is able to reduce the surface peak temperature exploiting the convection by redistributing the heat.
The vapour box divertor (VBD) configuration aims to create a stable plasma detachment by confining a dense lithium cloud in proximity of the divertor target. This can be possible thanks to the presence of several boxes which have different temperatures to determine Li evaporation or condensation. Large Li vapor density is required close to the target, while a low density is needed in the last box which is connected to the plasma chamber.
For the last configuration, the LMD should work in high recycling conditions with small evaporation. This can be possible by reducing the thermal resistance for the

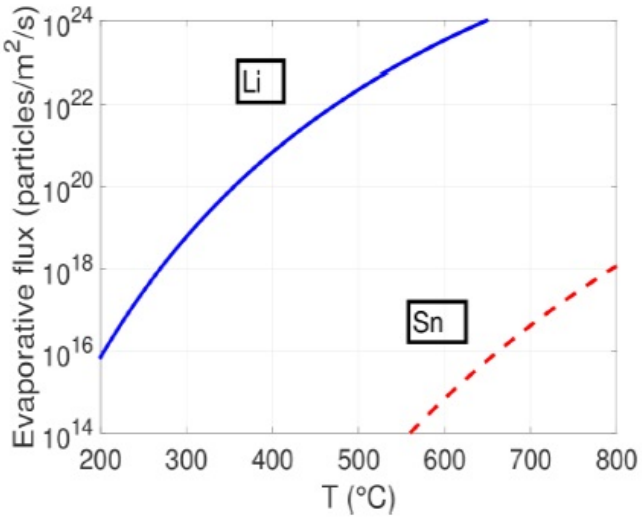

Figure 3.1: Evaporative flux as a function of temperature, Sn vs Li [9].

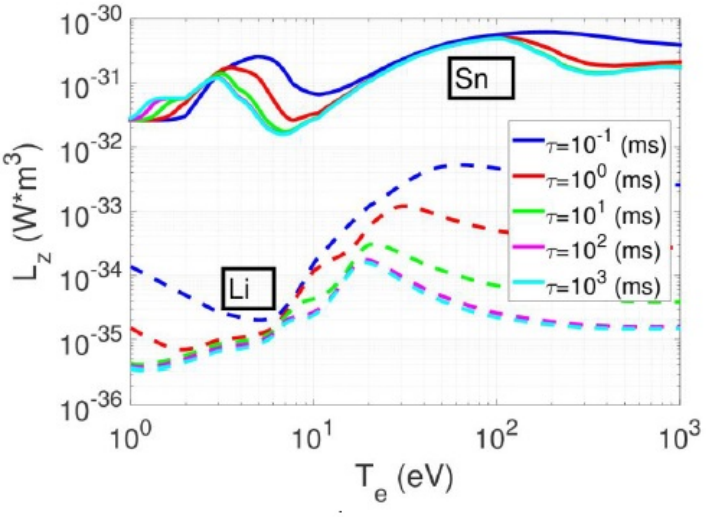

Figure 3.2: L_z as a function of temperature for different residence times. Li data are taken from [10], while Sn data come from [11].

heat transport to the coolant in order to keep a low surface temperature for PFMs. These divertor configurations foresee the use of a CPS as plasma facing surface. The CPS exploits the capillary force to prevent splashing phenomena and the ejection of liquid metal droplets while passively replenishing the target. This porous structure allows to obtain a homogeneous redistribution of the liquid metal on surfaces ensuring it a better confinement. Additionally, the absence of thermo-mechanical

stresses inside the CPS and between the CPS and the underlying solid layer can assure a longer divertor lifetime and a better flexibility to transient events.
LMDs must be designed in order to carry out the conventional divertor functions which include the heat and particles exhaust, the ash removal, the conformity with plasma scenario and the compliance with in-vessel components also allowing the remote handling. The presence of a liquid metal adds other requirements that are linked to the constant cooling of the CPS substrate, the constant replenishment of the plasma facing surface and the constant heating of the liquid metal in order to avoid freezing. Moreover, additional physical and chemical issues must be taken into account because exothermic reactions could arise in the case of contact between Li and water/air and materials can be eroded if the replenishment is not perfect. Materials can be corroded by the contact with a high temperature liquid metal, so the LMD design is not straightforward and a significant plasma contamination resulting from the emitted metal must be considered.

3.4 General characteristics of a Lithium Vapor Box Divertor

A Vapour Box Divertor (VBD) is a physical device able to reduce the high heat loads and particle fluxes coming on the divertor. This system is constituted by several chambers which can retain neutral particles increasing the number of collisions with plasma and resulting in an exchange of momentum and energy.
The first configuration for the lithium VBD was proposed by Goldston and it was characterised by solid substrate surfaces covered with liquid lithium by means of a CPS [12]. This configuration foresees the interaction between the lithium vapor and the plasma in order to cool it by taking advantage of radiation, ionisation and elastic collisions. These type of interactions aims to decrease plasma temperature in the divertor region leading to recombination (detachment conditions) and are able to spread plasma power over the VBD surfaces.
As previously mentioned, VBD chambers have different temperatures in order to provide different functions, i.e. the evaporation or condensation of the liquid metal. Moreover, the use of a lithium vapor instead of a non-condensable gas puffing has important implications for what concerns the impurity inventory and its spatial distribution. Indeed, a gas puff system needs a proper pumping mechanism, with a comparatively small efficiency, to remove impurities from plasma, while a vapor can be condensed on cool surfaces with an efficiency near to 100%. In the case of Li, for instance, the temperature of the condensing surfaces must be around $500°C$. Thanks to this fact, there is also the possibility to limit the quantity of lithium entering the main plasma region.
Furthermore, lithium cooling properties are more effective for plasma temperatures

below 5 eV compared to possible non-condensable gases injected, such as neon or argon. Additionally, Li injection can be performed at a higher rate due to the spatial limitation of the vapor cloud in the VBD chambers. Lithium, finally, has a low atomic number ($Z = 3$), so it cannot cause a strong radiative cooling, including Bremsstrahlung, in the core plasma region.

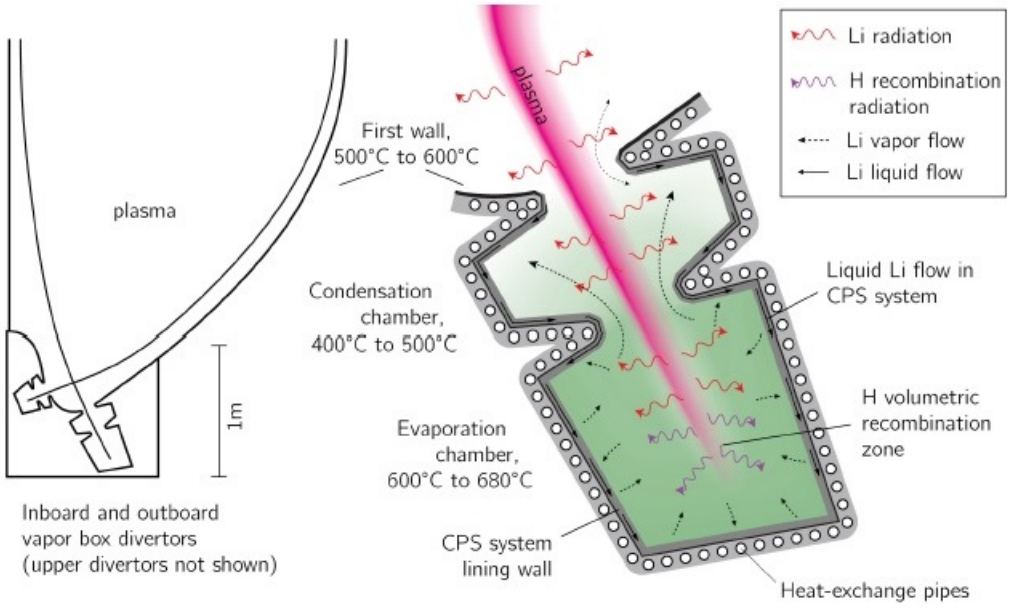

Figure 3.3: Illustration of a Lithium Vapor Box Divertor for a tokamak case [13].

3.5 LMD experiments in tokamaks and LPDs

The LMD research is one of the most active branch in the nuclear fusion field and the feasibility of this technology has been demonstrated thanks to many experiments which include tokamaks and LPDs. For the first, there are several experimental machines around the world, while, for the latter, the attention will be focused on Magnum-PSI and its predecessor, Pilot-PSI, located in the Netherlands.
In 2010, an experimental campaign was carried out on the National Spherical Torus Experiment (NSTX), a tokamak situated in Princeton. These experiments had the aim to test a molybdenum Liquid Lithium Divertor (LLD) surface by studying the deuterium retention when the divertor surface was refreshed after the Li evaporation. The key point was to control plasma density thanks to the lithium capability to absorb atomic and ionic deuterium through the formation of strong chemical bonds. In this way, deuterium was not able to recycle at the

device walls and different plasma operations can be studied. This campaign made a comparison between the LLD module performances, where Li evaporated thanks to the presence of two Lithium Evaporators (LITERs), and the results obtained with lithiated graphite covering the entire lower divertor [14].
Experiments related to the power exhaust have been accomplished in the Compact Assembly (COMPASS) tokamak, located at the Institute of Plasma Physics of the Czech Academy of Sciences in Prague, where performances of a LMD module based on a CPS have been studied. In this experimental campaign, the CPS was filled with two different liquid metals, Li and a LiSn alloy, in order to investigate damages at the porous structure. Moreover, the parallel heat flux was in the range 20-30 MW/m^2, while the perpendicular one reaches values up to 12 MW/m^2. The CPS was built on a molybdenum block and was constituted by Mo wires. Since LiSn has an higher evaporation temperature, its LMD module also includes a ceramic block to decrease the heat conductivity allowing a higher temperature in order to reach the LiSn evaporation. Results were very promising, since no CPS damage was observed for both metals and no contamination of the core and SOL plasma by Sn was noticed. In the case of Li, the CPS showed the bending/uplifting of the outer molybdenum layer leading to the CPS dry-out for heat loads between 16 and 18 MW/m^2. This problem did not occur for LiSn, but the heat flux was kept below 12 MW/m^2 [15].
The possibility of a LMD with liquid tin was studied for the first time in a diverted tokamak configuration in the Axial Symmetric Divertor Experiments (ASDEX) Upgrade tokamak, located at the Max Plank Institute for Plasma Physics in Garching. Here a liquid tin module (LTM) was tested in order to observe the presence of Sn in the SOL and main plasma. This module was characterised by a solid tungsten bulk connected to a tungsten porous sintered layer. Experiments, carried out by adopting several plasma parameters, showed the formation and the consequent ejection of Sn droplets leading to great erosion, bigger than the expected one. Furthermore, the CPS showed a leakage of tin [16].
Similar experiments were made in the Frascati Tokamak Upgrade (FTU), where liquid tin was adopted as plasma facing component. In this case, the module was exposed to a heat load of 18 MW/m^2 resulting in no damage for the CPS and no significant erosion of Sn. Additionally, FTU experimented a liquid lithium limiter, the Cooled Lithium Limiter (CLL), constituted by a CPS made of tungsten layers. This configuration withstood a heat load of 2 MW/m^2 for 1.5 s showing no damage and neither Li droplet emission [17].
Performances of the CPS filled with lithium have been studied in the T-11M tokamak during a Russian experimental campaign. Also in these experiments, the porous structure was applied at a limiter case and thermal loads, Li erosion and accumulation were investigated. This study foresaw a heat flux of 10 MW/m^2 with a discharge duration of 0.1 s resulting in a low contamination of Li in the plasma

centre and a reduction of the thermal flux impacting on the limiter. The CPS did not fail and it managed to retain lithium over a long operational period, while the main cause of erosion was related to ions sputtering for temperature lower than $500°C$ [18].
Finally, experiments on LPDs must be taken into account. In this context, liquid metal-based plasma facing components have been investigated in two devices, Pilot-PSI and Magnum-PSI. These devices are able to reproduce heat loads and plasma conditions expected in ITER and DEMO, such as the high electron density and the short collisional path lengths which lead to the ionisation of recycled and eroded particles and their consequent redeposition. Both Li and Sn performances have been observed by studying their erosion, the power handling and the vapour shielding. For a Sn-based CPS-type design, experiments demonstrated the possibility to withstand a 20 MW/m^2 heat flux thanks to the presence of CPS layer above a tungsten component actively cooled. In this situation, the limiting factor was related to the temperature, due to the presence of a CuCrZr pipe. However, the real limitation is given by the admissible Sn concentration in plasma which determines the erosion flux. The vapor shielding phenomenon for tin did not play a significant role due to the high required temperature, but it can be relevant in with off-normal heat loading. For the design including lithium, a strong interaction with deuterium was observed. This can reduce the erosion rate and, by combining it with a high redeposition rate, the maximum tolerable surface temperature can increase also rising the power handling. For both the metals, a surface temperature locking due to the liquid metal evaporation, direct radiation and plasma-vapor interaction was noticed [19].

Chapter 4

Magnum-PSI and the Lithium Vapor Box Module

4.1 Magnum-PSI device

Linear Plasma Devices (LPDs) can be applied to reproduce plasma conditions similar to those expected in tokamak reactors, so they are fundamental to study particles fluxes and heat loads that can be sustained by a crucial component like the divertor. In this framework, Magnum-PSI, located at the Dutch Institue For Fundamental Energy Research (DIFFER), is an example of a LPD which is able to recreate density, temperature and fluxes that are predicted in the near divertor region for ITER operations. Thanks to this device, studying SOL plasma mitigation and testing divertor components could be very effective and more undemanding, if compared to the tokamak structure and operations, since plasma can be set in a more rapid and controllable way. However, results obtained thanks to Magnum-PSI have to be extended to the tokamak case where geometrical factors play a not negligible role.

4.1.1 Magnum-PSI features

Magnum-PSI (MAgnetized plasma Generator and NUMerical modelling) is constituted by three different chambers: source (I), beam dump (II) and target chamber (III). A cascade-arc source, placed in the first chamber, generates hydrogen plasma which is confined into a beam by an axial magnetic field induced by a large superconducting magnet located around the structure. Plasma directly impacts the divertor target which is supported by a specific holder inside the target chamber. Skimmers, separating the chambers, prevent neutral particles, produced by the source, from

reaching the target chamber, thereby maintaining pressure independence regardless of the quantity of gas injected into the first chamber. Additionally, a system of differential pumping maintains dissimilar pressure values in the chambers thanks to the presence of three sets of pumps (P). Electron density and temperature can be evaluated by a Thomson Scattering (TS) measurement system placed in correspondence of the vertical green lines, as shown in figure 4.1. Target holder and source are retractable, so the respective distance from the TS system can be modelled to measure plasma conditions at different locations.

Gas is injected at different flow speeds into a proper chamber of the cascade-arc

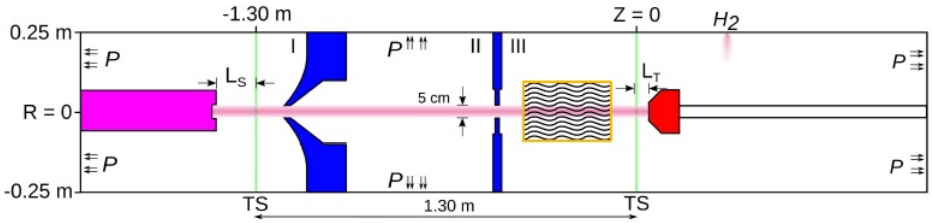

Figure 4.1: Scheme of Magnum-PSI [20].

source, where a tungsten cathode, connected to a DC power supply, is placed. Thanks to the thermionic phenomenon, emitted electrons can ionise the gas generating plasma which crosses a discharge channel constituted by five copper cascade plates. At the end of this section, another metallic plate, with a dual function of anode and nozzle, is present. Each cascade plate is insulated from the others by means of boron-nitride spacers. The cascade plate potential is electrically floating and is determined by the plasma itself, leading to a stable discharge. A floating potential means that the potential *floats* to a value sufficient to maintain an equal flux of positive and negative species.

Since this type of source has a finite ionisation efficiency, an additional flow of neutral particles is needed in the vacuum vessel. This additional gas puff is fundamental, although the neutrals pressure in proximity of the target must be determined by recycling effects in order to simulate ITER-like conditions. Due to this fact, gas dynamics has to be properly controlled and neutral particles must be removed before reaching the target by means of the pumping mechanism mentioned above.

The target is supported by retractable target holders which can be of two types: the Large Target Holder and the Multi-Target Holder. The first one is able to hold big targets which replicate the ITER divertor mock-ups, made of tungsten. The latter can accommodate five circular targets which are alternatively exposed to the plasma beam. Target holders are realised in stainless steel and are characterised by a great flexibility, since they can rotate $\pm 120°$ around its axis and tilt up to $90°$,

reproducing the plasma incidence angles typical of a nuclear fusion device divertor. Magnum-PSI also shows another chamber, called *Target Exchange and Analysis Chamber* (TEAC), which allows for the target investigation without compromising the internal vacuum and contaminating the surface.
In this device there are three types of diagnostics which include surface diagnostic in the target chamber, surface diagnostic in the TEAC and plasma diagnostic. In the framework of this thesis, the most relevant diagnostic is related to the Thomson Scattering, which can measure electronic density and temperature.
Thomson Scattering consists of the elastic scattering between a photon coming from a laser, so an electromagnetic radiation, and a charged particle, in this case an electron from plasma. This type of interaction is related to a photon energy which is higher than the hydrogen ionisation energy, but lower than the electron rest energy. Analysing the curve of the scattered radiation, that is a function of the wavelength, it is possible to obtain some important plasma quantities, like electronic density and temperature. The total scattered intensity corresponds to a measure of the electrons density, while the electrons temperature is measured from the Doppler shifted scattered spectrum. The TS beam enters plasma by means of diagnostic ports allowing measurements in two regions of the device: in front of the target and in front of the source. When the number of electrons is too low, the TS mechanism cannot collect data related to density and temperature since a poor number of photons is scattered, leading to a low detected intensity signal. Moreover, the cross section associated with the Thomson Scattering is not big and other sources of electromagnetic radiation can prevail over the TS signal.

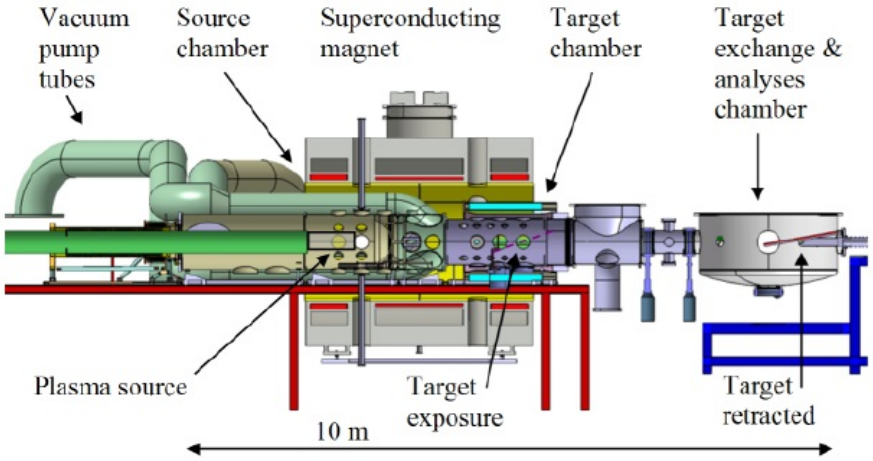

Figure 4.2: Schematic view of the experimental set-up of Magnum-PSI [21].

4.2 The lithium Vapor Box Module for Magnum-PSI

The lithium Vapour Box Module (VBM) adopted in Magnum-PSI has the aim to test the generation of a dense lithium vapor, its interaction with the plasma beam, the inducement of volumetric detachment and the redistribution of the power in the divertor region. The goals of VBM experiments are to simulate the vapor cloud-plasma interactions and to study the lithium transport towards colder surfaces where it can be condensed, leading to the liquid metal recirculation. Previously, detachment conditions were reached on Magnum-PSI by using lithium-coated targets. In these divertor configurations, Li is evaporated, or sputtered, from the target into the plasma beam where it radiates and becomes ionised. The power reaching the target is reduced by directly acting in the hottest part of this component thanks to radiation and to the latent heat of evaporation of the metal. Li can also be re-deposited on the target due to the plasma stream.
Conversely, in the VBM configuration, lithium enters plasma in the cross-field region, i.e. upstream with respect to the target, and it can be transported downstream due to plasma entrainment effects. In this way, Li ionises in the outer plasma region starting to cool plasma here and not in the central part of the beam which is hotter. Moreover, the quantity of evaporated liquid metal is externally controlled. Therefore, the lithium vapor is not generated by the heat deposited by the plasma, but it arises by setting a proper temperature on the evaporating surfaces.
Since lowering plasma temperature can not be sufficient, the vapor box must induce recombination thanks to volumetric processes in order to reduce the heat flux on the target. This phenomenon is related to an experimental formula [22] for the heat flux of a hydrogen plasma which reaches a tungsten target:

$$q = \Gamma_i(5.03T_e + 14.5eV) \tag{4.1}$$

Γ_i is the ions flux, while T_e is the plasma temperature.
For a plasma characterised by a temperature of few eV, the ions flux has an important role in the heat flux towards the target, so the VBM must also be able to reduce Γ_i by means of volumetric recombination.
The VBM is characterised by three cylindrical boxes made of stainless steel. Each box has two apertures so that it can be crossed by the plasma beam. The central one (CB) is responsible of the Li evaporation because it contains a lithium reservoir which is constantly heated by an external heating system, while the side boxes aim to limit the amount of Li flowing in the plasma chamber. There are two side boxes, one upstream (USB) and the other downstream (DSB), which are colder than the central one in order to re-condense lithium. Moreover, two optical diagnostics allow to access plasma in order to measure temperature and density. Finally, the plasma beam ends on a target made of tungsten which is located downstream the VBM.

Heat loads on this last component can be measured thanks to the presence of a calorimetry and thermocouples.

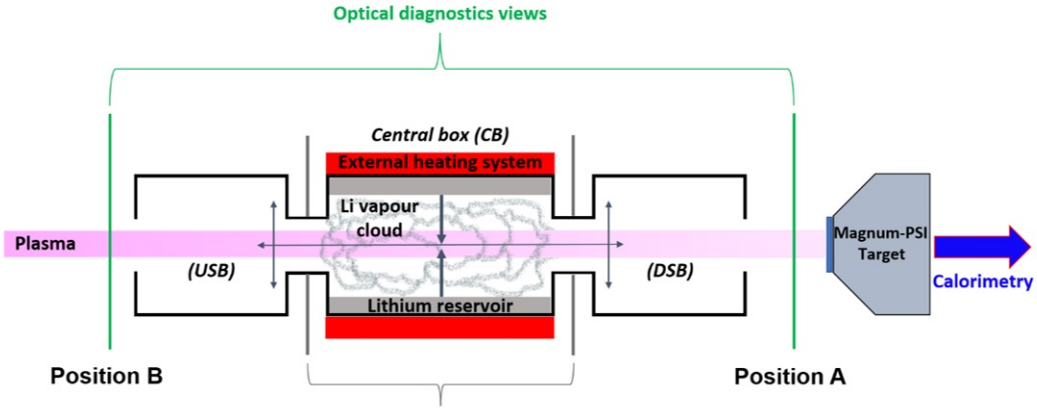

Figure 4.3: Schematic view of a VBM for Magnum-PSI. Here, the central box (CB), the upstream side box (USB) and the downstream one (DSB) can be visualised. Furthermore, the plasma path in the VBM is shown [23].

The VBM design

Many parameters have to be taken into account in order to design the VBM for Magnum-PSI correctly [24]. The first step consists of estimating the rate of lithium atoms needed to induce plasma recombination. This can be made by selecting a Li gas flux and a length along the plasma beam such that lithium atoms will affect the beam at that rate. This length corresponds to the central box length, while the lithium flux is associated to an evaporation temperature T_{evap}.
To determine the amount of Li needed for plasma recombination, the upstream power P_u of the plasma beam must be considered. Recombination phenomena occurs at low temperatures (below 1 eV) that can be reached when:

$$P_u \leq 2\pi r_p l_{CB} \epsilon_{cool} \Gamma_{Li}(T_{evap}) \tag{4.2}$$

r_p is the plasma beam radius, l_{CB} is the central box, so the length on which the Li vapor impinges, Γ_{Li} is the lithium flux and ϵ_{cool} represents the power removed by each Li atom interacting with the plasma beam.
A typical total beam power for Magnum-PSI is 3 kW, which needs to be reduced to 1.5 kW due to the action of lithium supplied by the VBM. The main plasma cooling processes involved in setting ϵ_{cool} are the elastic collisions between plasma particles and neutral Li, lithium ionisation and radiation due to Li electrons excitation. In Magnum-PSI, ϵ_{cool} can vary within a wide range of values. A conservative

estimate of 5.4 eV, corresponding to the first ionisation potential of lithium, is often considered.
By fixing P_u and ϵ_{cool}, the product $r_p l_p \Gamma_{Li}$ must be investigated.
Firstly, the attention can be focused on the plasma radius r_p. This value corresponds to the length at which an incoming Li atom is ionised and it can be calculated thanks to the following relation by assuming that a Li atom has crossed a ionisation mean free path radially at a distance equal to r_p.

$$1 = \int_{r_p}^{\infty} \frac{1}{\lambda_{mfp}(r)} dr \tag{4.3}$$

λ_{mfp} is the ionisation mean free path and it is defined as:

$$\lambda_{mfp} = \frac{\langle v \rangle}{\langle \sigma v \rangle_i T_e n_e} \tag{4.4}$$

where $\langle v \rangle$ is the average velocity for a Li particle and $\langle \sigma v \rangle_i$ is the Li ionisation rate coefficient.
Finally, two free parameters are left: the length of the central box and the lithium flux which depends on the evaporation temperature.
The experimental setup fixes a range for the temperature which goes from 800 K to 1000 K resulting in different conditions for plasma-lithium interactions. Starting from the evaporation temperature, the lithium flux can be found thanks to the Langmuir's evaporation law [25]:

$$\Gamma_{Li}(T_{evap}) = \frac{p_{Li}}{\sqrt{2\pi k_B T_{evap} m_{Li}}} \tag{4.5}$$

where m_{Li} is the lithium atomic mass, k_B is the Boltzmann constant and p_{Li} corresponds to the Li vapor pressure, which is defined as follows [26].

$$\ln(p_{Li}) = 26.89 - \frac{18880}{T_{evap}} - 0.4942 \ln(T_{evap}) \tag{4.6}$$

The central box length is selected according to the amount of lithium injected in the central chamber. Thus, the choice of this parameter represents a trade-off with the evaporation temperature and, as a consequence, of the vapor density.

Chapter 5

The SOLPS-ITER code

In the plasma boundary and SOL region, many complex physical phenomena take place, so numerical models are necessary to investigate edge plasma physics and plasma-wall interactions.
In the framework of this analysis, two different models have to be considered: a fluid model, which describes the plasma evolution, and a kinetic neutral transport model, that refers to neutral particles typically present inside a nuclear fusion device. The code being used in this field is SOLPS-ITER which stands for *Scrape-Off Layer Plasma Simulation for ITER*. This code, developed by the ITER Organization, is able to couple the fluid and the kinetic model in order to simulate transport phenomena affecting plasma in the SOL region. SOLPS-ITER consists essentially of a suite of heterogeneous codes developed by many people and institutions over the years, and it is currently maintained by ITER and the Max Planck Institute for Plasma Physics (IPP, located at Garching).

5.1 SOLPS-ITER structure

Since SOLPS-ITER takes advantage of a certain number of packages, a brief description of these tools will be shown in order to make an overview of the parts of the code adopted for this thesis.

- **DivGeo**: it is primarily designed for setting up the input files that are required for simulating the boundary of magnetic fusion devices. This package consists of a graphical interface where inputs of a specific case can be manually added. DivGeo needs an equilibrium configuration for magnetic flux surfaces, which refers to a particular experimental scenario. Magnetic flux surfaces must intersect only the divertor target in order to set the simulation domain.

- **Carre**: it is the part of the program responsible to generate the curvilinear

rectangular grid for B2.5, so the so-called *physical domain*. This is the domain of the simulation and it differs from the *computational domain*, where numerical calculations are carried out. See 5.2.2.

- **Triang**: it is the tool which creates the triangular mesh adopted by B2.5-EIRENE in the coupled mode.
- **B2.5**: it is the computational multi-fluid part of the code that solves transport equations for plasma.
- **EIRENE**: it is the Monte Carlo code to solve the transport of neutrals.

5.2 B2.5 and Eirene

SOLPS-ITER can describe SOL physics thanks to the use of two different models which can be properly coupled: a fluid model, related to the plasma conditions, and a kinetic model, applied to the study of neutral particles transport.
B2.5, whose original author was B. Braams, is the main plasma solver and it is based on a 2D fluid code where the fundamental equations involved are the continuity equation, the momentum conservation and the energy conservation for all the ion species.
B2.5 is written in *FORTRAN 90* and it is based on the finite volume discretisation method. At each time step, momentum conservation, continuity and energy conservation are solved thanks to the computation of volumetric and surfaces terms. This procedure foresees a number of *internal iterations* to relax the equation solutions before moving to the next time step (*external iteration*).
EIRENE, developed by D.Reiter, is responsible for solving the kinetic transport equation for neutral particles exploiting a Monte Carlo approach, so it refers to a statistically relevant number of particles in order to determine the distribution function. This code can properly represent both atoms and molecules.
EIRENE, like B2.5, is written in *FORTRAN 90* and it has as a main input a file called *input.dat*, which is an output of DivGeo after the use of *triang*. The *input.dat*, as it will be shown later, is made of several blocks that can be manually adjusted to simulate a specific case.

5.2.1 Physics involved in B2.5

B2.5 equations are based on Braginskii's equations which give a fluid description of the plasma [27]. This set of equations is derived in curvilinear orthogonal coordinates which include two different reference frames: the dynamical and the geometrical frame. Both are characterised by a radial component in the cross-field direction, but they show differences for what concerns the choice of the other

coordinates. The dynamical reference frame follows plasma particles along magnetic field lines, while the geometrical one is related to the projection of the magnetic field lines on the poloidal plane. Braginskii's equation will be shown in a simplified notation in this section [28],[29],[30].
Considering a pure hydrogen plasma with neutral particles and a static magnetic field, which is known, the plasma transport problem shows ten unknowns: ion density, ion and electron temperature, ion flow velocity components, current density vector components and the electrostatic potential. Equations that have to be solved are the conservation equations, related to the particle density, energy and momentum of ions and electrons, and the Poisson equation. In B2.5, quasi-neutrality is assumed, so electron density is equal to the ion one ($n_e = m_i$).
The continuity equation, for ions and electrons, is written as follows:

$$\frac{\partial n_e}{\partial t} + \nabla \cdot (n_e \mathbf{V}_e) = S_{n_e} \tag{5.1}$$

$$\frac{\partial n_i}{\partial t} + \nabla \cdot (n_i \mathbf{V}_i) = S_{n_i} \tag{5.2}$$

where S refers to the particles source term. Adopting the dynamical reference frame, it is possible to write the parallel (i.e. along magnetic field lines) momentum equation. Since ions and electrons masses are very different ($m_i/m_e \approx 2000$), inertia can be neglected in the electron momentum equation. Thus:

$$\begin{aligned}\frac{\partial}{\partial t}(m_i n_i v_{i//}) + \nabla \cdot (m_i n_i V_i v_{i//}) = \\ - \nabla_{//} p_i - (\nabla \cdot \Pi_i)_{//} + Z_i e n_i (\mathbf{E} + \mathbf{V}_i \times \mathbf{B})_{//} + R_{i//} + S_{m_i v_{i//}}\end{aligned} \tag{5.3}$$

$$-\nabla_{//} p_e - (\nabla \cdot \Pi_e)_{//} + e n_e (\mathbf{E} + \mathbf{V}_e \times \mathbf{B})_{//} + R_{e//} = 0 \tag{5.4}$$

The momentum equation for electrons is also known as the generalised Ohm's law. In these equations m represents the particle mass, n the density, $\mathbf{V}$ the velocity, p the pressure, $\mathbf{E}$ the electric field, $\mathbf{B}$ the magnetic field, Π the viscosity tensor, e the elementary charge and Z_i the atomic charge. Then, there are two terms related to friction: $S_{m_i v_{i//}}$ is the loss of momentum due to friction between ions and neutrals, while R is the ion-electron friction. This last term consists of:

$$R_e = -R_i = e n_e \left(\frac{\mathbf{j}_{//}}{\sigma_{//}} + \frac{\mathbf{j}_{\perp}}{\sigma_{\perp}}\right) - 0.71 n_e \nabla_{//} T_e - \frac{3}{2} \frac{e n_e^2}{2 \sigma_{\perp} B^2} \mathbf{B} \times \nabla T_e \tag{5.5}$$

where $\mathbf{j}_{//}$ and $\mathbf{j}_{\perp}$ are the current densities in the parallel and perpendicular direction with respect to the magnetic field lines.

The same considerations hold for $\sigma_{//}$ and $\sigma_{\perp}$ which represent the electric conductivities.
The ion-electron friction term also includes losses caused by the Ohmic heating, friction of electrons with different temperatures in a direction parallel to $\mathbf{B}$ and deflection of electrons with a temperature gradient orthogonal to the magnetic field.
The total current density can be obtained by summing ion and electron momentum equation, as follows.

$$\mathbf{j} = e(Z_i n_i \mathbf{V_i} + n_e \mathbf{V_e}) \tag{5.6}$$

This formulation includes several components:

$$\mathbf{j} = \mathbf{j_{dia}} + \mathbf{j_{in}} + \mathbf{j_{vis}} + \mathbf{j_s} + \mathbf{j}_{//} \tag{5.7}$$

In this last equation, $\mathbf{j_{dia}}$ is the diamagnetic current due to the pressure gradient, $\mathbf{j_{in}}$ is the contribution related to the inertia and gyro-viscosity, $\mathbf{j_{vis}}$ is the current driven by the parallel viscosity and $\mathbf{j_s}$ is the current associated with the ions-neutrals friction.
Another important quantity is the perpendicular velocity which affects the radial transport of particle.

$$\mathbf{V}_{\perp} = \mathbf{V}_{\perp}^{\mathbf{a}} + \mathbf{V}_{\perp}^{\mathbf{dia}} + \mathbf{V}_{\perp}^{\mathbf{in}} + \mathbf{V}_{\perp}^{\mathbf{vis}} + \mathbf{V}_{\perp}^{\mathbf{s}} + \mathbf{V}_{\perp}^{\mathbf{an}} \tag{5.8}$$

The first term on the right hand side consist of the sum of different contributions which are the $E \times B$ drift and the diffusive and thermo-diffusive velocities. The other components are referred to the diamagnetic velocity, the inertia and gyro-viscosity term, the viscosity contribution and the ion-neutral friction. The last term represents the anomalous velocity which can be defined adopting the anomalous diffusion coefficient D_{an}:

$$\mathbf{V}_{\perp}^{\mathbf{an}} = -D_{an}^{n} \frac{1}{n} \nabla n - D_{an}^{p} \frac{1}{n} \nabla p \tag{5.9}$$

where the first term is the density-driven diffusion, while the second one corresponds to the pressure-driven one.
Finally, the total energy balance for ions and electrons can be written:

$$\frac{\partial}{\partial t}\left(\frac{3}{2} n_i T_i + \frac{m_i n_i}{2} \mathbf{V_i^2}\right) + \nabla \cdot \left[\left(\frac{5}{2} n_i T_i + \frac{m_i n_i}{2} \mathbf{V_i^2}\right) \cdot \mathbf{V_i} + \Pi_i \cdot \mathbf{V_i} + \mathbf{q_i}\right] = (Z_i e n_i \mathbf{E} - \mathbf{R_i}) \cdot \mathbf{V_i} - Q_{ei} + S_{Ei} \tag{5.10}$$

$$\frac{\partial}{\partial t}\left(\frac{3}{2} n_e T_e\right) + \nabla \cdot \left(\frac{5}{2} n_e T_e \mathbf{V_e} + \mathbf{q_e}\right) = -e n_e \mathbf{E} \cdot \mathbf{V_e} + \mathbf{R_e} \cdot \mathbf{V_e} - Q_{ei} + S_{Ee} \tag{5.11}$$

Here, $\mathbf{q}$ is the energy flux, Q_{ei} is the ion-electron energy exchange and S_E represents an energy source term.
This set of equations can be closed thanks to the presence of proper expressions for the transport coefficients (hidden in the perpendicular velocity formula) and for the heat diffusivity in the energy fluxes $\mathbf{q}$.

5.2.2 B2.5 grid

Since the topic of this thesis is related to model a linear plasma device, such as Magnum-PSI, differences between the plasma grids in the tomakak and LPD cases must be shown.
In a tokamak, there is the possibility to take advantage of the toroidal symmetry in order to reduce the model to two dimensions by using an orthogonal set of coordinates, for example those of the geometrical frame ($\mathbf{e}_\phi$,$\mathbf{e}_\theta$,$\mathbf{e}_\mathbf{r}$), where the toroidal component can be ignored. This results in a 2D grid for plasma where the coordinates are the radial and the poloidal ones.
Similarly, a two-dimensional grid is obtained also in LPDs by assuming cylindrical symmetry of the cylindrical plasma beam. The set of coordinates are ($\mathbf{e_r}$,$\mathbf{e_z}$,$\mathbf{e}_\theta$) which can be reduced to the axial-radial components (r,z) neglecting the rotation angle θ. It is worth to mention that, in LPDs such as Magnum-PSI, the cylindrical topology is not perfect near the plasma source, so a magnetic surface can show a slight bulge between the magnetic field coils (section 6.4). Moreover, in a cylindrical plasma beam, the density gradient is oriented along the radial direction and a radial electric field can also be present.
The B2.5 approach for the discretisation is based on the Finite Volume Method applied on a topologically rectangular mesh which follows magnetic surfaces. In this framework, conservation equations, written in this section, can be considered as a set of convection-diffusion equations:

$$\nabla \cdot (\rho \mathbf{u} \Phi - \Gamma \cdot \nabla \Phi) = S \tag{5.12}$$

This is a general form where the quantity Φ is a scalar unknown, while $\mathbf{u}$ is an unknown velocity quantity. S is the source term. Φ refers to the centre of each cell, while $\mathbf{u}$ is discretised at the cell faces. Then, once all the equations are discretised, the iteration on each time-step starts in a cyclic order to obtain the steady-state converged solution, so the state where plasma parameters have no big variations in time. The method for the time discretisation is an implicit one, so the solution is considered at each next time step.
The B2.5 grid stores the magnetic field components, B_θ and B_ϕ, in the centre of each cell. Since the cells are aligned with the magnetic field, the poloidal direction can be derived from the node positions of a cell, while the toroidal one is orthogonal to the poloidal plane. For tokamaks, the toroidal component is much bigger than

the poloidal one, while B_ϕ is zero for LPDs [31].
The code is able to reproduce the computational domain mesh thanks to the definition of cut positions in the mesh of the physical domain, which depend on the topology of magnetic surfaces. Considering the case of a lower single-null configuration for a tokamak, there is only one cut, in proximity of the X-point, along which the physical domain is opened up to create a rectangle. In this way, three different regions, related to the SOL, core and PFR, can be obtained in the mesh.
For what concerns LPDs, the procedure is similar, but the grid can be seen as a simplification of the tokamak one, since only the part devoted to the SOL is present.
In the figure 5.1, it is possible to observe the transformation from the physical domain to the computational one for a tokamak case. In detail, the light blue area points out the SOL sheath edge region for the inner divertor, while the green area is related to the outer one. The orange line separates the SOL and the PFR, while the black line represents the separatrix, dividing the SOL from the core plasma region. The yellow and red borders refer to the computational domain adopted in LPDs. The first acts as the plasma source and marks the eastern boundary, as it can be observed in the figure on the right, while the black dotted line is the symmetry axis located at the southern side of the beam. Additionally, the northern side is the plasma beam edge and the western one depicts the LPD target. Clarifications of the domain will be shown in 6.4, where the Magnum-PSI domain for B2.5 is submitted.
Finally, one important difference between tokamaks and LPDs is found in the plasma transport. In tokamaks, plasma crosses the separatrix, starting from the core, due to radial transport mechanisms which determine its presence in the SOL region and in front of the target. Instead, for LPDs, plasma is transported from the source to the target, which are in front of each other, and this results in different boundary conditions.

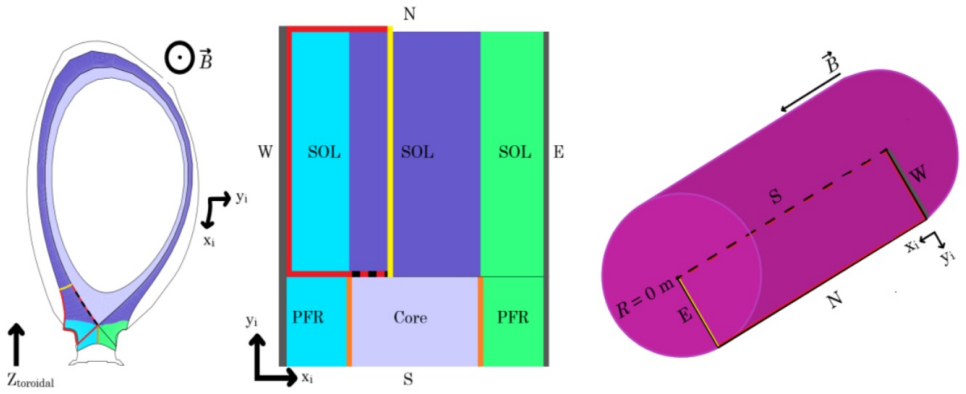

Figure 5.1: Physical domain of a tokamak adopting a lower single-null topology (left), computational domain implemented in SOLPS-ITER (centre) and LPD domain (rigth) [32].

5.2.3 Physics involved in EIRENE

EIRENE is responsible of the kinetic treatment of neutral species, so atoms and molecules in the SOL, solving the Boltzmann transport problem by means of a Monte Carlo method. This method is able to reproduce very complex geometries making a precise analysis of a system at the kinetic level. Since Monte Carlo considers a statistically relevant number of particles, it reproduces a great number of *Monte Carlo histories*, so the computational time can be very large in order to reduce the statistical noise.
The dynamics of plasma is given thanks to the kinetic theory which aims to find the distribution function for each plasma species following a ensemble of plasma particles. Particles are characterised by a certain mass and electric charge and they can interact which each other by means of collisions. These processes do not alter the total number of particles and neither the total momentum or kinetic energy, so these quantities are called *collision invariants*.
The distribution function $f(\mathbf{r}, \mathbf{v}, t)$ depends on the time t and on the phase space $(\mathbf{r}, \mathbf{v})$. Considering $f(\mathbf{r}, \mathbf{v}, \mathbf{t})d\mathbf{r}d\mathbf{v}$, it is possible to notice that this term corresponds to the number of particles in the elemental phase space volume, meaning that it represents the particles density in the phase space. Due to this fact, the evolution of the distribution function follows the behaviour of a continuity-type equation, so the rate of change of the number of particles present in $d\mathbf{r}d\mathbf{v}$ is given by the divergence of the particles flux and by a source term. After some algebra, the evolution of the distribution function can be written as follows [6]:

$$\frac{\partial f}{\partial t} + \mathbf{v} \cdot \nabla f + \mathbf{a} \cdot \nabla_v f = \left(\frac{\partial f}{\partial t}\right)_c \tag{5.13}$$

where ∇ refers to the space derivatives, while ∇_v to the velocity ones. The last quantity is the collision term, while $\mathbf{a}$ is the particle acceleration.
Starting from (5.13), the collision term can be written as the sum of pre and post-collision integral, considering a collision as a discontinuous process.

$$\left(\frac{\partial f}{\partial t}\right)_c = \int \sigma(\mathbf{v}', \mathbf{V}'; \mathbf{v}, \mathbf{V})|\mathbf{v}' - \mathbf{V}'| f_a(\mathbf{v}') f_b(\mathbf{V}') d\mathbf{v}' d\mathbf{V}' d\mathbf{V} - \int \sigma(\mathbf{v}, \mathbf{V}; \mathbf{v}', \mathbf{V}')|\mathbf{v} - \mathbf{V}| f_a(\mathbf{v}) f_b(\mathbf{V}) d\mathbf{v}' d\mathbf{V}' d\mathbf{V} \quad (5.14)$$

Where f_a is the distribution function for a test particle, f_b the one for a background particle and σ is the cross-section for a binary collision where $\mathbf{v}'$ and $\mathbf{V}'$ are the velocity of the test particle and of the background one before the collision and $\mathbf{v}$ and $\mathbf{V}$ those after the collision process. Motion between collisions is considered as free and the distribution function for the background particle is assumed to be known.
Equation (5.13) can be written in the following way if the collision term is included in the Boltzmann equation:

$$\frac{\partial f_a(\mathbf{r}, \mathbf{v}, t)}{\partial t} + \mathbf{v} \cdot \nabla_v f_a(\mathbf{r}, \mathbf{v}, t) + \Sigma_{t,a}(\mathbf{r}, \mathbf{v})|v| f_a(\mathbf{r}, \mathbf{v}, t) = \int C(\mathbf{r}, (\mathbf{v}', a'; \mathbf{v}, a))|\mathbf{v}' - \mathbf{V}'| f_a(\mathbf{v}') d\mathbf{v}' + Q(\mathbf{r}, \mathbf{v}, t) \quad (5.15)$$

where $\Sigma_{t,a}(\mathbf{r}, \mathbf{v})$ is the total macroscopic cross-section, $C(\mathbf{r}, (\mathbf{v}', a'; \mathbf{v}, a))$ represents the kernel of the collision operator and $Q(\mathbf{r}, \mathbf{v}, t)$ is the primary source. The macroscopic cross-section is defined as:

$$\Sigma_{t,a} = \frac{1}{\lambda_{t,a}} = \frac{|\mathbf{V}|}{\nu_{t,a}} \quad (5.16)$$

where $\lambda_{t,a}$ is the mean free path and $\nu_{t,a}$ represents the collision frequency, so the number of collisions experienced by a test particle during a unit time interval.

$$\nu_{t,a} = \sum_k \nu_{k,a}$$

$$\nu_{k,a} = \int \sigma_k(\mathbf{v}, \mathbf{V}, a; \mathbf{v}', \mathbf{V}', a')|\mathbf{v} - \mathbf{V}| f_b(\mathbf{V}) d\mathbf{v} d\mathbf{V} d\mathbf{V}' \quad (5.17)$$

The index k refers to a certain type of collision process that a given species a can make.
Equation (5.15) describes the evolution of the distribution function of the particles generated by the source term Q. A particle travels along straight lines and then collides with the background one or with the wall of the physical domain changing its

velocity. This process lasts until the particle is absorbed. Based on the meaning of (5.13), Monte Carlo methods solve the transport equation reproducing this process for a finite number of trajectories, so adopting the *analog sampling* technique.
This type of Monte Carlo code is defined by two different parts. The first one refers to the *geometry module*, which performs the particle tracking, while the second consists of the *physical module*, that is related to the specific physics of the problem and depends on the definition of the source term and on the collision frequency.
Finally, the collision concept can be introduced. Collisions are a Monte Carlo process that adopts random numbers to establish when particles collide, which type of process develops and how the velocity vector changes after the collision. The most general form to identify a collision is:

$$a + b \rightarrow c + d(+e) \tag{5.18}$$

where the letter a indicates the test particle and b is used for the background one, c, d and e are the products of the reaction. Products can be neutrals, so the simulation continues, or charged particles, leading to a source for B2.5. Every neutral-plasma collision results in source and sink of particles, ion momentum, ion heat and electron energy that can be sent to B2.5.
Collisions can be divided in two groups.

- Elastic collisions: kinetic energy and momentum are conserved, so zero-net loss of energy. In this case, only the velocity vector of the interacting species can change.
- Inelastic collisions: kinetic energy is not conserved, so the species of the colliding partners change. This is the case of ionisation and dissociation processes.

5.3 B2.5-EIRENE coupling and parallelisation

The procedure related to the coupling between B2.5 and EIRENE starts with the preparation of the numerical grid for the two codes. In the general case of a tokamak, this step is performed by means of the *triang* command that defines a closed line in the (r, z) plane to establish the vacuum chamber border and applies the triangularisation in the plasma rectangular grid and also in the vacuum region inside the vessel. At the end of this process, the two triangular grid are merged together to obtain the final grid. It is also important to underline that the Monte Carlo code, employed in EIRENE, solves the transport of neutral particles in 3D volumes of an arbitrary geometry, but, when the two codes are coupled, the toroidal dimension is ignored and the cell volume is computed considering a fixed length $d\phi$ along the toroidal coordinate.

After the preparation of the grid, sources and sinks must be computed into the fluid equations for each plasma species in terms of Monte Carlo responses, so evaluating the type of involved collisions.
Then, plasma equations can be solved, finding density, velocity and temperature distributions.
Finally, plasma distribution function is updated and employed in the evaluation of the collision processes by the Monte Carlo code.
In a coupled simulation, most of the computational time is taken by EIRENE due to the particles tracing, thus, to reduce the time of a simulation, a parallelisation scheme can be adopted. The parallelisation method employed by EIRENE is the MPI, which is able to uniformly divide all the test particles that have to be simulated over multiple processors. These processors share their results whit each other in order to calculate a new background, improving the efficiency of the code. B2.5 works in one processor, the so-called *master processor*, while EIRENE takes advantage of a number n of processors. The master processor is also responsible of the coupling between B2.5 and EIRENE. Firstly, only B2.5 is simulated and the other processors are not operating. When the first plasma background is calculated, the master processor transmits this state to the other processors in order to run an EIRENE cycle. In this way, a new neutral background is established and another B2.5 iteration can be performed. This process lasts until the number of required time steps is reached.

Chapter 6

Simulation set-up

In this chapter, assumptions and settings of the SOLPS-ITER modelling of a VBM for Magnum-PSI will be shown. This part of the thesis contains an explanation of the inputs file used for B2.5-EIRENE coupled simulations starting from the description of the model adopted in DivGeo, where some important operations have to be taken into account to represent a LPD correctly. Then, an overview about the mesh generation will be carried out to clarify the computational domain. Finally, all the modifications needed for EIRENE will be introduced in order to understand every type of collisions and involved particles in plasma-lithium interactions.

6.1 B2.5 geometry

B2.5 is the module responsible for the geometry generation and the plasma grid that must be adopted in DivGeo. This module creates the file *b2fgmtry* which includes all the cells needed to represent the plasma beam. The starting point for the cells generation consists of the file *b2.grid.parameters* that must be edited to obtain the proper Magnum-PSI conditions. This file contains data about the dimension of the domain, the position and the number of coils (N) needed to generate the magnetic field. Starting from the value of the magnetic field is possible to calculate the current which crosses each winding of the coils. The magnetic field $\mathbf{B}$ is taken from experimental data and, for all these simulations, a value of 0.7 T is considered. The current is determined by evaluating both the magnetic field maximum allowable value within the Magnum-PSI superconductive magnets and current itself:

$$I = 257A \cdot \frac{\mathbf{B}}{2.5T} \tag{6.1}$$

Setting $\mathbf{B} = 0.7$ T, the current which crosses the coils (with N=5) is 71.96 A. Information about the cell size in the axial and radial direction must also be

defined. These values are contained in two different files that are linked to the *b2.grid.parameters*: the *fn-z* and *fn-r* files, which respectively refer to the axial and radial cell size profile.
Lastly, the number of elements for the two directions is present in the *b2ag.dat* file. The number of radial cells is 36 and the number of the axial ones is 150. Thanks to all these inputs, the *b2fgmtry* can be created by executing the command *b2run b2ag*. All the files needed for the plasma grid generation must be contained in a folder, called *baserun*, in order to be read by SOLPS-ITER.
To visualise the plasma grid on the DivGeo graphical tool, the *b2fgmtry* file has to be converted by means of the command *b2plot*. This procedure allows to create a file *.sno* exploiting a dummy standalone run, with no physical results. Files with this extension can be loaded in DivGeo together with the Magnum-PSI vessel geometry including the VBM.

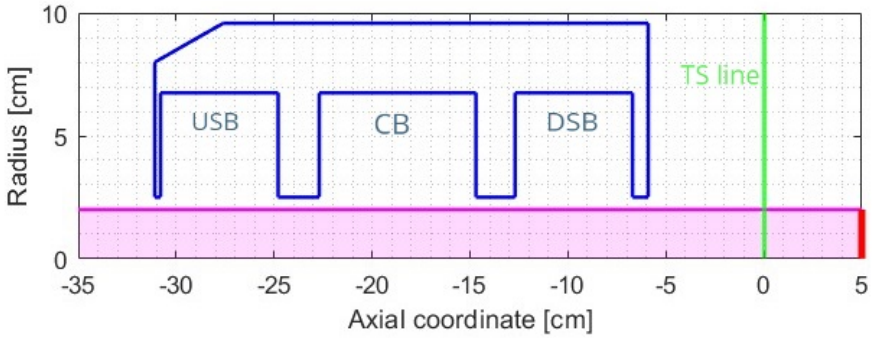

Figure 6.1: View of the VBM implemented in DivGeo. The magenta region corresponds to the plasma region, while the red line represents the target. The Upstream Side Box (USB), the Central Box (CB) and the Downstream Side Box (DSB) are shown together with the Thomson Scattering (TS) line in the target chamber.

6.2 Use of DivGeo

Since the device to be implemented is linear, some important operations must be carried out on the graphical tool in order to deal with the different configuration of LPDs with respect to tokamaks.

6.2.1 Divertor Targets

First of all, LPDs do not account for the presence of two divertor targets, so a fake tokamak equilibrium has to be imported to trick DivGeo into producing a case.
Two divertor targets, that intersect the tokamak equilibrium, must be manually added and selected as *Elements not for Eirene* in order to avoid problems with the real target of Magnum-PSI. Additionally, the section *Limiter and linear configurations* must be chosen to tell DivGeo that the case is linear. However, two targets must be properly created in the vessel configuration of Magnum-PSI and the one located at the Thomson Scattering line in the source chamber has to be modified to represent the device source. As discussed in the section 5.2.2, the grid in LPDs only accounts for the SOL region, so the private flux region (PFR) is not present. Since the definition of this region is needed in the *Target specification* in DivGeo, two surfaces must be manually created in proximity of the vessel ends. These fictitious surfaces represents the PFR edge for both the targets: they must be outside the plasma grid and they are ignored in the generation of the EIRENE grid.
In the *Target specification* section, for the real Magnum-PSI target, some important properties, like the target material, the wall temperature and the sputtering model, must be defined. In the specific model of this thesis, the target is made of tungsten and the wall temperature is 998 K, while the sputtering phenomenon has not been considered. In DivGeo, the temperature must to be set in eV, so a temperature of -0.086 eV is considered, where the minus sign guarantees a Maxwellian distribution adopted for the recycled particles in the Monte Carlo code.
In this section, the number of *Histories* has also to be specified. This value represents the number of neutral trajectories from plasma recycling that EIRENE will calculate. All these properties are also present for the second target, the one which is located in the source chamber, but the values are irrelevant, since the number of *Histories* is set to 0 in order to convert it in the plasma source.

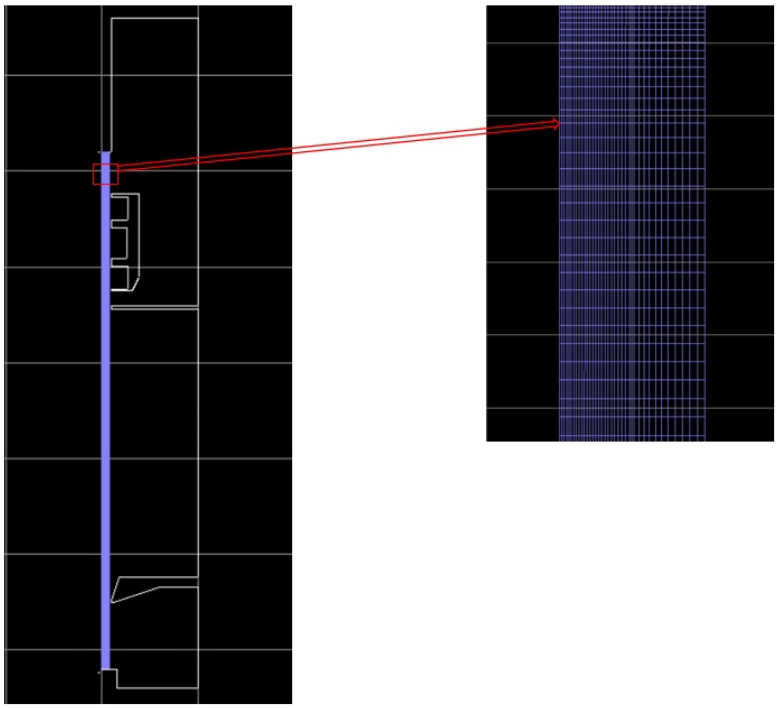

Figure 6.2: Magnum-PSI vessels and vapor box in DivGeo with an enlargement of the plasma grid in the target chamber

6.2.2 Plasma species

In DivGeo, it is essential to define plasma species in order to generate corresponding neutral species for EIRENE and ion species for B2.5. While the Magnum-PSI plasma beam in experiments mainly consists of hydrogen, the presence of lithium must also be considered. Liquid lithium evaporates from the central box and ionizes upon interacting with the hydrogen plasma. DivGeo automatically incorporates collision terms for hydrogen using various databases from SOLPS-ITER. However, this automated process does not extend to lithium. Only recombination and ionisation data from the ADAS database are included for this element. Hence, all other interactions involving lithium need to be manually added.

6.2.3 Vessel and VBM walls properties

Vessel and vapor box walls properties are defined in the section *General Surface Data*. Here, temperature, sputtering model and materials must be added.
For Magnum-PSI, the walls of the vessel are made of iron and the temperature is typically 300 K (-0.02585 eV) with the exception of the walls at the source,

which are at a temperature of 3000 K (-0.2585 eV), and that which corresponds to the target holder, with a temperature equal to the one of the target (-0.086 eV). Moreover, at the Thomson Scattering location in the source chamber, a vessel wall overlaps with the plasma grid requiring the definition of transparent properties. This can be performed by changing the *Surface Type* and *Surface Side* options to 0. For what concerns the vapour box, the walls are made of iron, but the temperature is different. Side walls have a temperature of 400 K, while the central ones, where Li evaporates, are at 800 K, which is the evaporation temperature set in the experiments.
The last important parameter in *General Surface Data* is the *Reflection model* adopted for the walls. All surfaces of the vessel exhibit identical values for the reflection model, with the exception of the pumping surfaces. The reflection model is set to 1, indicating that reflection data for particles and energy reflection coefficients are sourced from a SOLPS-ITER database named *TRIM*.

6.2.4 Pressure Feedback Loop

Walls which act as pumping surfaces to keep the proper pressure in the different chambers show a different value of the reflection model. Hence, a Pressure Feedback Loop (PFL) is chosen to represent these surfaces needed by Magnum-PSI. The PFL is activated in DivGeo by setting the *Reflection model* to 4. This value is able to modify the recycling probability of the selected walls and must be supported by two additional parameters: the *Reference cell* and the *Reference pressure*.
The reference pressure is related to the pressure in each chamber and is taken from experiments on Magnum-PSI. The source chamber usually has a high pressure, above 1 Pa, while the middle chamber shows a lower pressure, between 0.3 and 0.4 Pa. The pressure in the target chamber can change with the recycling flux of particle, so this value is not easy to set and it can vary. In the model implemented for this thesis, a pressure equal to 1.956 Pa is selected in the source chamber, while the middle chamber has a pressure of 0.412 Pa. Finally, the target chamber pressure is 0.3 Pa.
The reference cell for the PFL is unknown in DivGeo because the EIRENE mesh is not created yet. Thus, a value different to 0 must be chosen in order to ensure a different surface model for the pumping walls. Then, this parameter must be changed in the EIRENE files once the grid is generated.
The pumping surfaces in the target and in the source chamber are the back walls of the Magnum-PSI vessel, while the entire outer cylindrical wall is picked for the middle chamber. Pumping surfaces can be clearly seen in the figure 4.1.
Adding the PFL in proximity of the pump locations means to set a boundary condition for the absorption probability of these surfaces. In this way, the particles absorption probability can change during the simulation in order to keep a constant

pressure, equal to the values fixed in the three chambers.

6.2.5 Gas puffing

In the source chamber, a non-ionised gas flux of hydrogen is needed to properly represent the plasma source of the device, so a gas puff of H must be added to the simulations in order to properly simulate the cascade-arc source behaviour. This amount of gas is retained in the source chamber by the action of the skimmers, but it is able to interact with the plasma beam.
In DivGeo, it is possible to manually add the gas puff setting the *Gas species*, the *Particle energy* and the *Puffed flux*, after the selection of the *Puffing slot*, so the location of the gas puff. In the case of the source chamber, two surfaces have to be marked as gas puff: the first is in the plasma region (at the beginning of the beam) and the latter corresponds to the perpendicular wall.
The total hydrogen flux is given by:

$$\Gamma_{source} = 2\frac{\frac{\Gamma_{slm}}{22.4}N_{av}}{60} \tag{6.2}$$

where Γ_{slm} is the particles flow in *standard liter per minute* set in the experiments and N_{av} is the Avogadro number. The number 2, placed in front of the formula, is related to the introduction of atomic hydrogen and it is based on the assumption that H_2 gets dissociated in proximity of the source. Moreover, the gas flux coming from the puffing slot is not the same. Indeed, most of the hydrogen flux is injected in the parallel direction to the plasma beam (the 80% of the total), while the remaining part comes from the perpendicular surface selected as gas puff.
The experimental particle flow is 4 slm, so the contributions to the gas puff flux are $2.87 \cdot 10^{21}$ $\frac{particles}{m^2 s}$ in the parallel direction and $7.17 \cdot 10^{20}$ $\frac{particles}{m^2 s}$ in the perpendicular one. The particles energy is -0.2585 eV, which corresponds to the temperature of the walls at the source, and, also in this case, the minus sign is adopted to obtain a Maxwellian distribution.
Finally, a third gas puff must be added in DivGeo to simulate the flux of lithium coming from the central chamber of the vapour box. As previously anticipated in 4.2, the evaporation temperature can oscillate between 800 K and 1000 K and this affects the Li flux to the plasma beam. For this model, the evaporation temperature is 800 K, so the flux of lithium, calculated thanks to the Langmuir law (4.5), is $1.149 \cdot 10^{21}$ $\frac{particles}{m^2 s}$. The Li particles energy is -0.0689 eV, which represents the temperature set for the walls of the central box.

6.3 Creation of the EIRENE grid

The last parameters to be set in DivGeo are related to the creation of the EIRENE grid. This task can be carried out by selecting the option *TRIA-EIRENE parameters*. The elements of the vacuum vessels must be meshed from the inside, so a value of -1 must be picked, while all the elements of the vapour box assume a positive value. Then, the *General Triangle size*, equal to 3, has to be chosen to properly represent the grid for Magnum-PSI.
The command to create the EIRENE grid is *triang* and it must be launched from the baserun folder. The generation of EIRENE input files, like the file *input.dat*, the EIRENE run preparation, the triangularisation for the grid outside the plasma region and the action of merging the plasma mesh with the neutrals one are performed at different steps thanks to *triang*.
Additionally, this command can provide the exact values of the reference cells for the PFL by using the option *inquire* and sending the coordinates of the PFL elements. This procedure generates the reference triangle for the pumping surfaces in EIRENE.
The triangularisation process takes place also in the B2.5 where the fluid and neutral meshes overlaps: this region is characterised by a very high resolution for the grid.

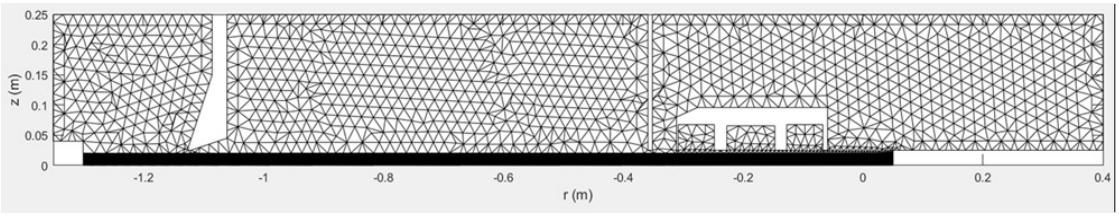

Figure 6.3: The EIRENE grid generated by *triang*

6.4 B2.5 domain and boundary conditions

As described in 6.1, the plasma domain only foresees the SOL region due to the configuration of LPDs and, in the case of Magnum-PSI, it extends from the Thomson Scattering at the source to the target holder. This is caused by the presence of a plasma expansion region in front of the cascade-arc source where a transition from the unmagnetised to the magnetised state takes place. Modelling this region is very difficult, so the source side of the domain has to be located at the Thomson Scattering position in the source chamber to avoid issues related to the plasma grid. Moreover, exploiting the symmetry of the plasma beam, just a half of the radial direction is represented, so the axis $r = 0$ is the symmetry axis. The entire domain is rectangular and four different sides can be identified in order to impose the correct boundary conditions.

The southern side corresponds to the symmetry axis, while the northern one

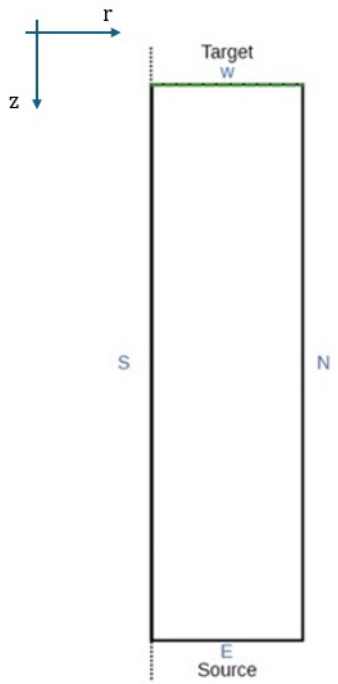

Figure 6.4: B2.5 domain of a LPD in SOLPS-ITER [33].

represents the plasma beam edge. The Magnum-PSI target is placed to the west, while the plasma source is in the eastern side. Boundary conditions refer to different quantities, like ion and electron energy, the electric potential, the continuity and the parallel momentum, and they have to be assigned on a specific file called

b2.boundary.parameters.
Three different plasma regions can be considered in Magnum-PSI: the plasma source region (near the cascade-arc source), the well magnetised region (the central part of the beam) and the sheath edge region (in front of the target). This subdivision allows to understand the boundary conditions imposed at the eastern and western side, so in proximity of source and target.
For the target side ($z = 0.05m$), a sheath edge condition (Bohm criterion) is applied for energy, momentum and continuity. The microscopic sheath is not resolved in the simulations due to the limited spatial resolution, but its effects are associated with the choice of the boundary condition. This results in zero gradient density, collective sound speed for charged particles that impacts on the target and the definition of the transmission coefficients (γ_e and γ_i) for the energy flux through the sheath. Additionally, the potential at the target is defined as floating, so it can change according to the electric conditions of the plasma. A floating potential means that the net current density at the target is zero, so the ions density current is equal to the electrons one. To correctly represent the floating potential, an initial guess value is assumed at the target. This quantity can be obtained from other models, based on similar conditions, and it must be updated with the most recent value every time the simulation restarts.
For the source side ($z = -1.3m$), the boundary condition refers to radial profiles of electron density and temperature that are taken from the Thomson Scattering measurements in the source chamber. Here, quasi-neutrality and $T_e = T_i$ are assumed. At this location, SOLPS-ITER requires an additional profile: the potential one. This profile cannot be easily determined in a theoretical way because it depends on several contributions related to the cascade-arc source of Magnum-PSI. Furthermore, the source potential affects the electric field $\mathbf{E}$ of the device leading to variations of the plasma Ohmic heating which can alter the plasma temperature [21].

$$\mathbf{j} = \sigma \mathbf{E} \tag{6.3}$$

$$P_{ohm} = \mu j^2 \tag{6.4}$$

$\mathbf{j}$ is the current density, σ is the electric conductivity, μ is the plasma resistivity and P_{ohm} is the power devoted to the Ohmic heating.
The potential profile, unlike the density and temperature profiles, is not measured from experiments, so it can be set in order to match the temperature profile of the simulation with the experimental temperature profile at the Thomson Scattering line in the target chamber.
Then, the northern boundary ($r = 0.02m$) is the location where the EIRENE grid and the B2.5 one start overlapping. The boundary condition is linked to the definition of the temperature and density decay lengths (λ_n and λ_T respectively) in order to obtain a decreasing exponential trend of plasma in the radial direction.

Specifically, these values represents the radial distance travelled by ions before they recombine into neutrals loosing most of their energy.
Finally, the southern side ($r = 0m$), which is the axis of symmetry, assumes zero flux boundary conditions for all the physical quantities.

6.5 Collision processes

The collision processes are automatically defined by DivGeo selecting the proper plasma species in the apposite section. All the collisions are listed in the file *input.dat*, where other parameters, like the cross section, are introduced. DivGeo accounts for all the interactions just for some specific plasma species, like H, by referring to databases present in SOLPS-ITER (HYDHEL, AMMONX and AMJUEL), while, for other elements, like lithium, just the recombination and ionisation are included on the database ADAS. Thus, all the other processes must be manually added in the file *input.dat*.
In the tables below, every collision process regarding hydrogen and lithium is listed.

Collision process	Type	Database
$e^- + H \rightarrow e^- + H^+ + e^-$	EI	AMJUEL 2.1.5
$H^+ + H \rightarrow H + H^+$	CX	HYDHEL 3.1.8
$e^- + H_2 \rightarrow H + H$	DS	AMJUEL 2.2.5g
$H + H \rightarrow H + H$	EL	AMMONX R-H-H
$H + H_2 \rightarrow H + H_2$	EL	AMMONX R-H-H2
$H_2 + H_2 \rightarrow H_2 + H_2$	EL	AMMONX R-H2-H2
$H^+ + H_2 \rightarrow H + H_2^+$	CX	AMJUEL 3.2.3
$e^- + H_2 \rightarrow H + H^+ + e^-$	DS	AMJUEL 2.2.12
$e^- + H_2^+ \rightarrow H + H$	DS	AMJUEL 2.2.14
$e^- + H_2^+ \rightarrow H^+ + H^+ + 2e^-$	DS	AMJUEL 2.2.11
$H^+ + H_2 \rightarrow H^+ + H_2$	EL	AMJUEL 0.3T
$e^- + H_2 \rightarrow e^- + H_2^+ + e^-$	EI	AMJUEL 2.2.9
$e^- + H_2 \rightarrow H + H^+$	DS	AMJUEL 2.2.10
$H^+ + e^- \rightarrow H(1s)$	RC	AMJUEL 2.1.8

Collision process	Type	Database
$e^- + Li \rightarrow e^- + Li^+ + e^-$	EI	ADAS SCD96
$H^+ + Li \rightarrow H + Li^+$	CX	ADAS CCD96
$H + Li^+ \rightarrow H^+ + Li$	CX	[34]
$Li^+ + e^- \rightarrow Li(1s)$	RC	ADAS ACD96
$H + Li \rightarrow H + Li$	EL	BGK
$H_2 + Li \rightarrow H_2 + Li$	EL	BGK
$Li + Li \rightarrow Li + Li$	EL	BGK
$Li^+ + H \rightarrow Li^+ + H$	EL	[35]
$H^+ + Li \rightarrow H^+ + Li$	EL	[35]
$Li^+ + Li \rightarrow Li + Li^+$	CX	[36]

It can be noticed that all the reactions in the second table just include the first stage of ionisation of lithium. This fact is caused by the reduced temperature range present in Magnum-PSI, so only Li^+ is considered as a plasma specie for B2.5.
The possible collision processes are: the electron impact ionisation (EI), the charge exchange (CX), the dissociation (DS), the elastic collision (EL) and the recombination (RC). All these reactions are fundamental to correctly simulate the behaviour of the vapour box and the Li-plasma interactions.
Additionally, each process has its own rate coefficient $\langle \sigma v \rangle$ which can be plotted as a function of the plasma electrons temperature. Analysing the rate coefficients is cardinal to understand all the plasma collision processes and it allows to explain the trend of certain plasma quantities, as it can be seen in chapter 7.

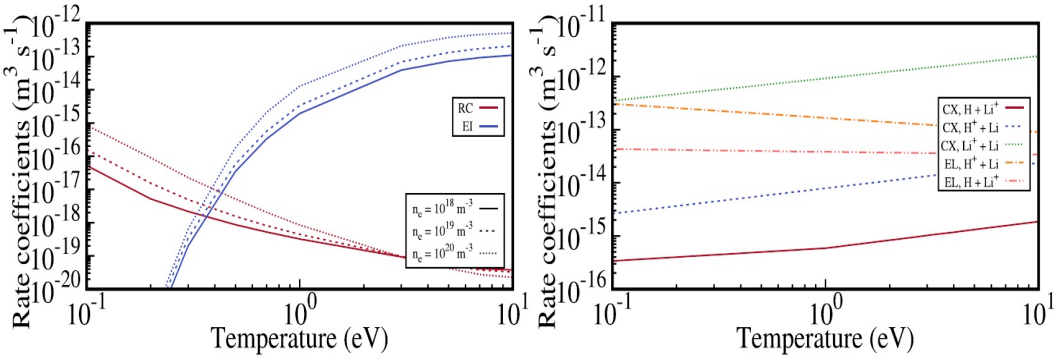

Figure 6.5: Rate coefficients of different collision processes for the temperature range of Magnum-PSI. On the right recombination and electron impact ionisation $\langle \sigma v \rangle$ are shown for H, while, on the left, rate coefficients for charge exchange and elastic collision between H and Li can be seen [20].

6.6 The file input.dat

As mentioned in the section 6.3, the command *triang* can generate the input file for EIRENE which is called *input.dat*. This file is the basic one for the kinetic treatment made by the Monte Carlo code, so it is full of content to correctly reproduce all the collision processes present in the plasma.
The file *input.dat* is composed by several blocks that are automatically generated based on the parameters set in DivGeo. Since lithium is not considered by SOLPS-ITER as a default plasma specie, some important modifications must be manually performed in order to simulate the behaviour of this element. Moreover, some changes must be carried out to model a LPD: transparent properties needs to be assigned to the surface representing the Magnum-PSI source by acting on the block 3*a* of *input.dat*.
The block number 4 contains all the collision process listed in the previous section. Here, every reaction which is not present in the databases must be added, including fit coefficients, cross sections and rate coefficients. These processes involve test particles and bulk particles which are listed in other blocks of the file. Also in this case, some modifications must be introduced in order to take into account all the colliding particles. Test particles are present in the blocks 4*a*, 4*b* and 4*c* and include both neutral and charged atoms (also molecules), while the bulk species are catalogued in the block 5*a*. The complete presence of particles in these blocks is fundamental to properly model the Li-plasma interactions. A crucial aspect concerns neutral lithium within the 4*a* block, as DivGeo overlooks the direct reflection of this element off the device walls. The reflection model must not be disregarded, because it impacts on the recycling processes of the plasma interacting

with the Li cloud coming from the VBM. Therefore, adjustments to the fast and thermal reflection parameters are necessary specifically for the line containing lithium in the file *input.dat*.
Another block, which includes important information about the device walls, is the number 6*a*. Here, all the surfaces with their relative temperature, reflection and sputtering model are listed. The first modification consists to change the index of the cell referring to the PFL, so the pumping surfaces. Then, the exact value of their absorption probability must be indicated. Moreover, lines related to the recycling probability, referring to all the plasma species, have to be added for every surfaces, except for the ones of the PFL. This value is different from zero just for the target surface and the central chamber of the vapour box, where Li evaporates. Lastly, other blocks contain information about the number of particles to be simulated by EIRENE, thus the gas puff location and characteristics are present, including the volumetric recombination for hydrogen and lithium.

Chapter 7

Results and discussion

In this chapter, all the results of the lithium VBM modelling with SOLPS-ITER are shown. Plots are obtained thanks to specific MATLAB programs able to post-process the fundamental plasma quantities obtained during the simulations. All the useful plasma information are contained in a file called *b2fstate*, which represents the last plasma state calculated by SOLPS-ITER.
Different simulations have been carried out in order to reach a proper convergence in terms of plasma parameters, like the temperature and density at the target location. To complete this task, the RECYCT values for the PFL, in the file *input.dat*, and the target potential have been updated every time a simulation restarts. More precisely, before modelling the behaviour of the VBM holding Li in the central chamber, simulations of the vapour box with no lithium have been performed. In this way, plasma can reach an equilibrium point without the presence of lithium respecting the procedure that is experimentally followed in Magnum-PSI. Then, this plasma state is recorded becoming the initial state for simulations where Li evaporation is activated. Thus, results can be analysed and changes between the two cases can be observed.
The two VBM models implemented on SOLPS-ITER also differ in terms of particles absorption probability at the pumps. For the one not including Li, the PFL is correctly set by selecting the proper *Reflection model* and the RECYCT value is updated to start again the simulation. For the case with Li, the PFL is disabled and the absorption probability of the pumping surfaces is kept constant and always equal to the previous model. This procedure aims to reproduce the behaviour observed during the experiments. Indeed, adding lithium, the pressure in the three chambers changes if the pumps works at a constant speed.
Lastly, for both the models the potential value at the target is always updated with the most recent quantity until the convergence is reached. This can be done by changing the value POTPAR(1,2) in the file *b2.boundary.parameters*.

7.1 Plasma and neutral particle density

In this section, the density of each plasma species is analysed and a comparison between the models with and without lithium is performed in order to understand how Li affects the plasma beam density.
Quantities coming from B2.5, so electron and ion density, have been averaged on the plasma beam volume. A similar procedure is required for the neutral density, e.g. H^0, Li^0 and H_2. In this case, their domain is extended to all the Magnum-PSI vessel, thus the average on the plasma volume has to be carried out after an interpolation in the axial direction at different values of the plasma radius. Additionally, the domain of the plots does not include the entire plasma beam, but it is reduced to the target chamber, where the VBM is located.
One of the main functions of the vapor box is to retain neutral particles, leading to an enlargement of plasma-neutral collisions. Neutral particles that join these processes are not just constituted by Li^0 coming from the evaporation surface in the central box, but atomic hydrogen also appears due to the capability of the VBM to reflect H particles deriving from volumetric recombination and recycling phenomenon. Then, neutral hydrogen can recombine in H_2 on the vapor box walls being thermally reflected inside the module.
Figures 7.1a and 7.1b refers to the electron and H^+ (proton) density. In both cases, the model without Li shows a trend which is just slightly perturbed by the VBM presence. Indeed, e^- and H^+ density curves have a smooth decreasing tendency approaching to the target, where electrons and protons recombine generating a sudden dump, which indicates the presence of neutral hydrogen.
A completely different situation can be observed for the case including lithium. Here, the plasma beam starts interacting with Li which is injected by the upper wall of the central box. Firstly, protons and electrons collide with the lithium cloud which is at a temperature much smaller than the plasma one (i.e. the evaporation temperature of 800 K). Due to this temperature difference, the evaporated liquid metal is heated up by collision processes and it is subsequently dragged by the plasma beam towards the target.
In this framework, one of the most relevant processes is the charge-exchange mechanism between Li^0 and H^+. This results in an increase of Li^+ density and in a reduction of that of plasma protons (H^+) starting from the central box of the VBM, as it can be noticed in figure 7.3. In this picture, a comparison between Li^0 and Li^+ density can be seen. As it is possible to expect, the peak in the neutral lithium density is reached in the central box, where Li is introduced with an evaporation flux of $1.149 \cdot 10^{21}$ $\frac{particles}{m^2 s}$. Here, part of Li^0 begins to interact with protons coming from the plasma, resulting in the formation of ionised lithium. Li^0 can also condense on the walls of the vapor box which are at a temperature lower than the plasma one.

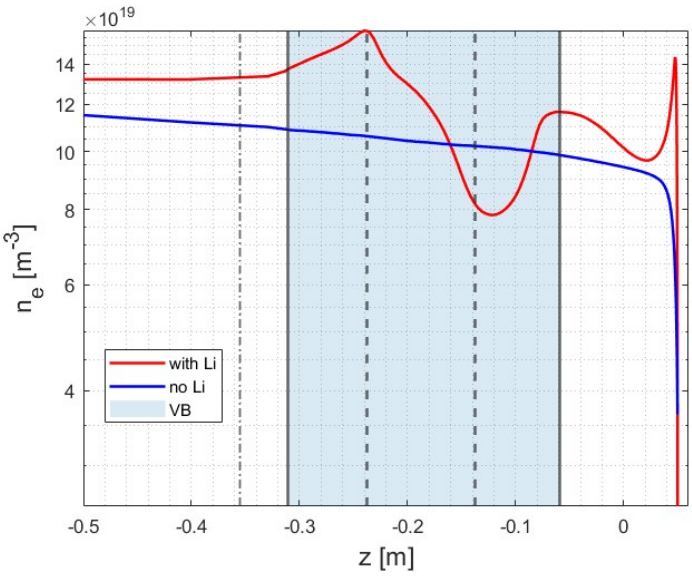

(a) Electron density

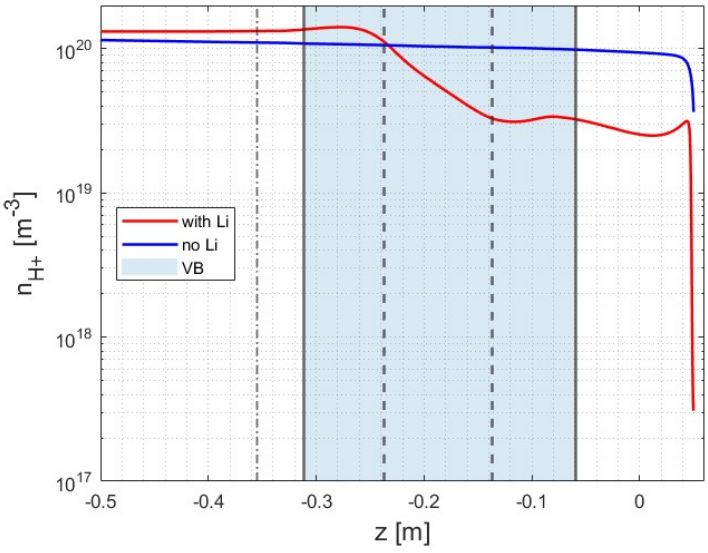

(b) H^+ density

Figure 7.1: Plasma density in term of proton (H^+) and electron density

In the side box located on the right, neutral lithium density starts to decrease leading to a boost in Li^+ density. This trend is related to the electron impact ionisation which involves plasma electrons and neutral lithium. Li shows a lower first ionisation potential with respect to hydrogen, thus it can be more easily ionised

and excited. This behaviour can be confirmed by looking at the electron density, which gets bigger following the Li^+ density trend.
Between the side box and the target, Li^+ dominates over neutral lithium, while this tendency is reversed at the target. At this position, Li^+ density decreases, while that of Li^0 starts to grow again. This can be explained by the presence of the recycling phenomenon, so Li^+ recombines at the wall being reflected as a neutral lithium. Additionally, reflected Li^0 can ionise in front of the wall and be prompt redeposited on this surface. This phenomenon justifies the slight peak of the Li^+ density in front of the target surface.
Li^0 density is also indicated in figure 7.2. This picture gives a more precise view of the neutral lithium density trend by showing a 2D plot of the target chamber vessel. The biggest presence of Li^0 is found in the central box where the surface from which it evaporates can be clearly seen. Neutral lithium moves reaching the plasma beam and collision processes firstly begin at the plasma edge. Then, lithium is entrained by the plasma and its transport towards the target can be explicitly observed. Moreover, a region with a lower particle density is found between the side box on the right and the target. On one hand, the presence of this region may arise from the ionisation of Li^0 originating from the recycling phenomenon. On the other hand, it may result from the side box function of retaining neutral particles escaping from the central one. However, the low resolution in this area could be attributed to a small amount of particles simulated by EIRENE in that location. By looking at this plot, it can be evident that the downstream side box is the one which retain the biggest amount of neutral lithium. Furthermore, just a small fraction of Li is able to escape upstream due to the reduced temperature gradient in Magnum-PSI.
The presence of the vapor box generates an inversion between plasma species, so

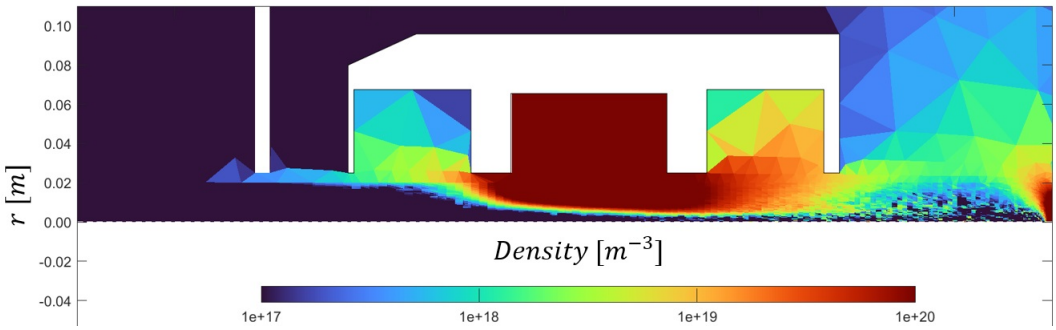

Figure 7.2: Two dimensional distribution of neutral Li density inside the target chamber

Li^+ starts dominating on H^+. In figure 7.4a, the turning point of this process can be visualised at $z = 0.2\ m$. This phenomenon is caused by the charge-exchange

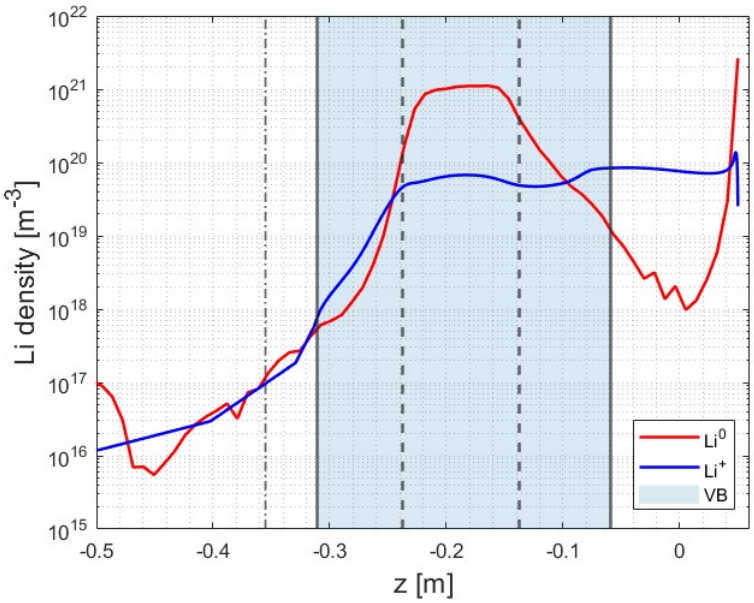

Figure 7.3: Distribution of Li density

mechanism, between H^+ and Li^0 that acts together with the electron impact ionisation mentioned above. Plasma species inversion can also be visualised in terms of H^+ and Li^+ energy density by multiplying the ion density, the Boltzmann constant and the ion temperature read from the *b2fstate*. Thus, it is possible to confirm this phenomenon by observing the plot of this quantity, which is shown in 7.4b. The turning point is always at the same axial coordinate and, starting from this location, Li^+ assume the highest content of plasma energy.

The capability of a VBM to retain neutral particles is showed in figure 7.6, where a comparison between the case with Li and without Li has been carried out. Both models retain neutral hydrogen coming from volumetric recombination and recycling at the target, but a big difference in terms of H^0 density is observed, see figure 7.6a. The recombination between plasma protons and electrons, coming from lithium ionisation, is the mechanism responsible of this behaviour and it acts alongside the charge-exchange between Li^0 and H^+. This phenomenon results in a higher H^0 density, especially in the central box, to the detriment of a H^+ density reduction, as previously stated for the plasma species inversion point. Moreover, the increase of neutral hydrogen density also affects the molecule density inside the VBM (figure 7.6b). Indeed, the possibility of H^0 atoms to recombine at the vapor box walls increases resulting in a raise of H_2 density. In this way, the VBM reduces the number of molecules that are pumped away by the pumping system of Magnum-PSI retaining H_2 which can interact with the plasma beam.

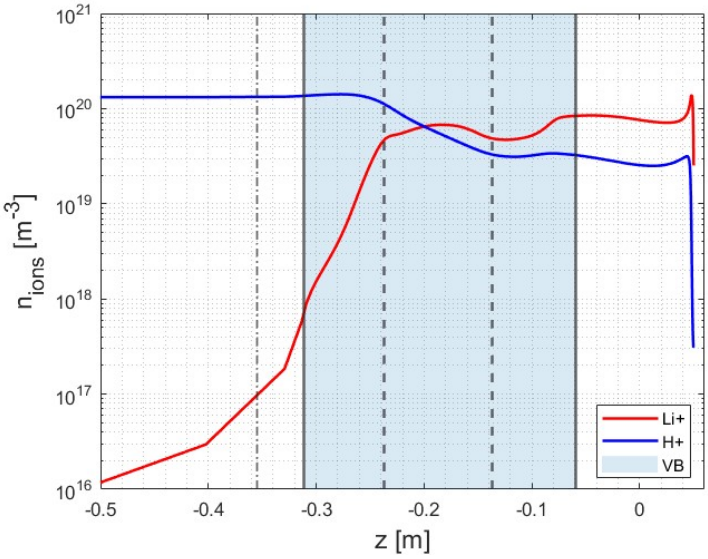

(a) H^+ and Li^+ particle density

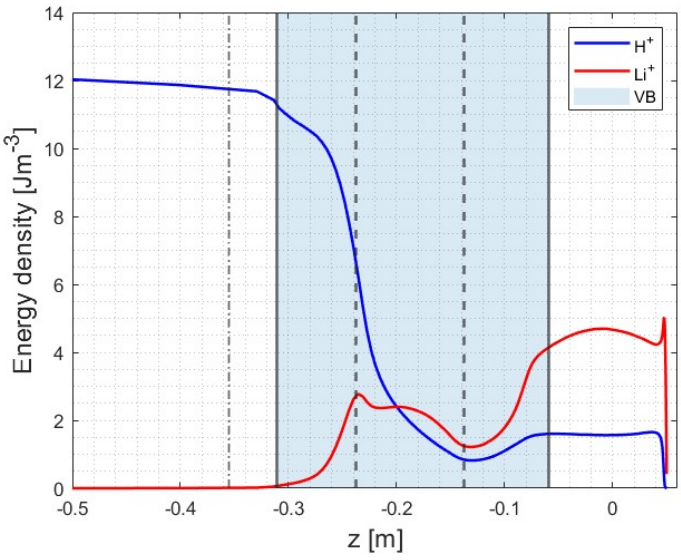

(b) H^+ and Li^+ energy density

Figure 7.4: Inversion of plasma species in terms of Li^+ and H^+ particle and energy density

The presence of atomic hydrogen in the plasma beam can be better visualised by looking at a 2D plot where the entire target chamber vessel is shown. H^0 density for the model including Li is depicted in figure 7.5. The action of the VBM and

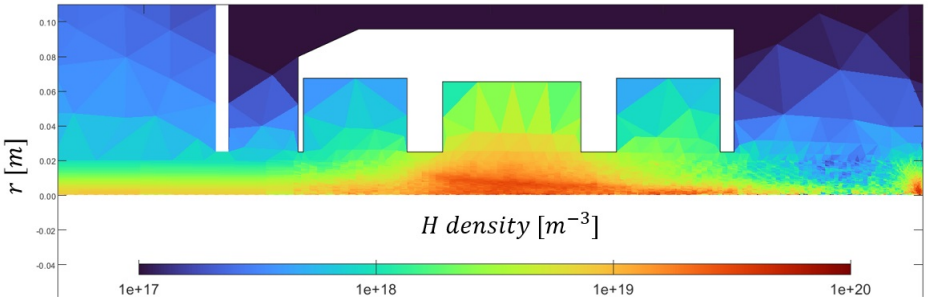

Figure 7.5: Two dimensional distribution of atomic hydrogen density inside the target chamber

the lithium influence can be noticed in proximity of the central chamber where an increase of atomic hydrogen is present. This behaviour indicates that the vapor box is correctly retaining neutral particles in order to increase the energy and momentum transfer. Furthermore, a high density region of H^0 is located in front of the target confirming the recycling phenomenon of H^+ particles into neutral ones, which are then re-emitted.

7.2 Plasma and neutral particle temperature

Plasma temperature is shown in this section in terms of electron temperature. Also in this case, an average on the plasma beam volume has been performed and a comparison between the case including lithium and the one without lithium can be seen.

The presence of the VBM combined with lithium evaporation induces a large reduction of the electron temperature, especially in the central chamber. In this location, plasma interacts with the lithium cloud starting to loose energy. Electron temperature begins to decrease in the side box on the left, reaching its minimum in the central one, where most of the processes involving Li occurs. In the entire VBM, the temperature range is between 0.5 eV (at the entrance of the vapor box) and 0.19 eV in the region between the central chamber and the box on the right. At these low temperatures, the recombination involving plasma protons (H^+) and electrons occurs causing the reduction in the electron and H^+ density, as shown in figure 7.1. The dominant collision processes between plasma and neutrals are found in the charge-exchange and elastic collision between H^+ and neutral Li. Both phenomena determine a transfer of momentum and energy from plasma particles to lithium. The first process is also responsible of the Li^+ and H^0 density growth in the central box, while the second one does not alter the global energy content of the involved particles. Furthermore, the electron impact ionisation is able to decrease

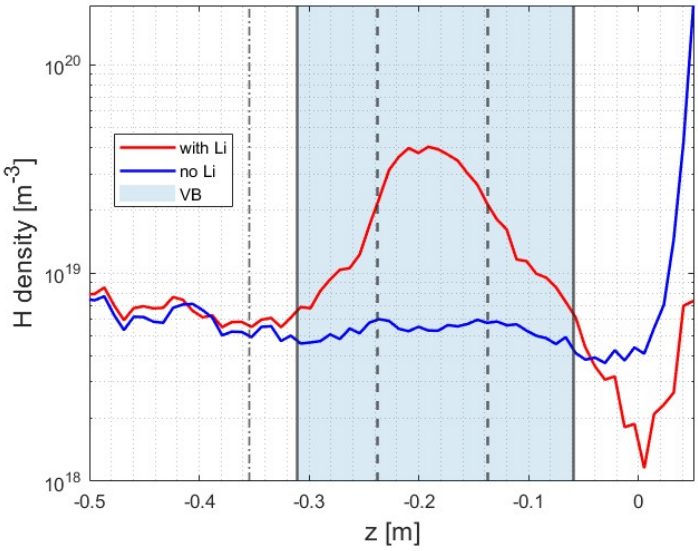

(a) H^0 density

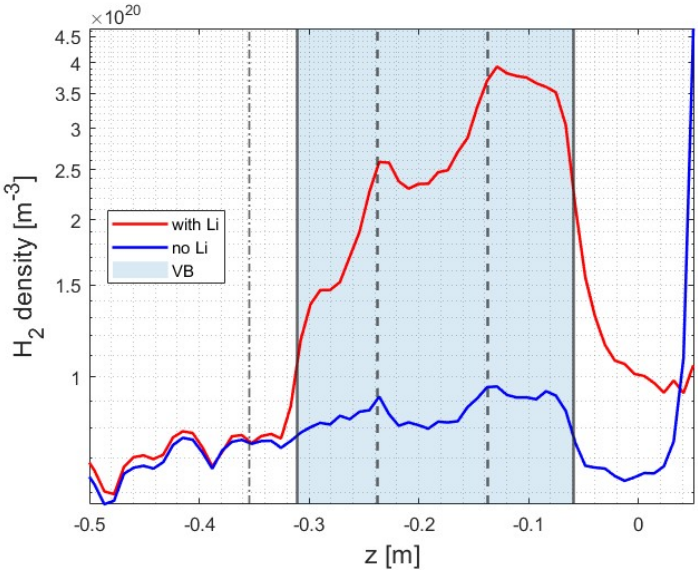

(b) H_2 density

Figure 7.6: Hydrogen atomic and molecular density in the target chamber

the electron temperature, as electrons from plasma expend energy to ionise neutral lithium. In this context, the electron impact ionisation with H^0 could be related to the slight increase of H^+ density in the side box on the right. Here, the electron temperature starts rising.

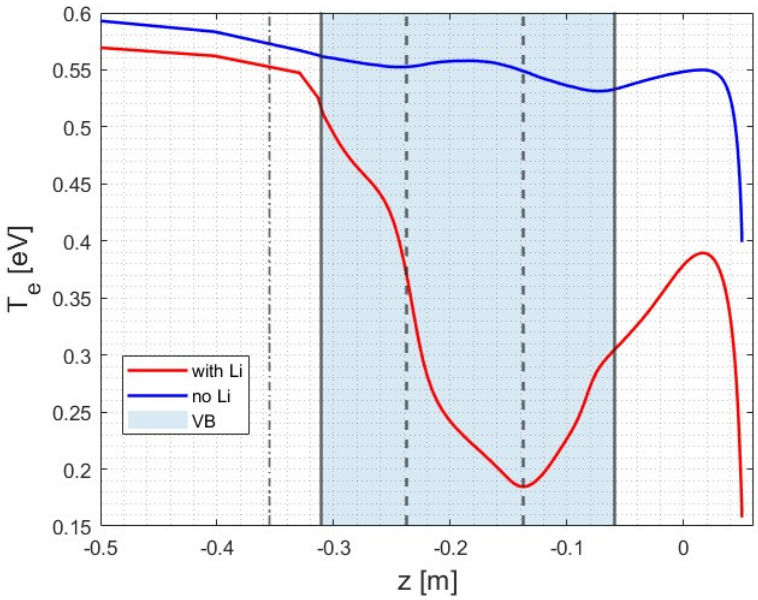

Figure 7.7: Distribution of the electron temperature inside the target chamber

The temperature increase begins at the entrance of the downstream side box and holds till the target location, where recycling occurs. This phenomenon is peculiar and can be justified by looking at the temperature and density of neutral species (figures 7.2, 7.5 and 7.8).
As previously highlighted, one of the primary functions of the VBM is the retention of neutral particles, thus neutral lithium and hydrogen are kept within the three chambers of the device. Specifically, plasma entrains neutral lithium which is retained in the downstream side box, where a considerable density is found (between 10^{19} and 10^{20} m^{-3}). Similarly, atomic hydrogen follows a comparable pattern: while the majority of H^0 is contained within the central box, a significant density also permeates into the downstream chamber (around 10^{19} m^{-3}). Here, the temperature of neutral species, approximately 0.4 eV, exceeds that of the electrons inside the central box of the VBM. Hence, hotter neutral particles are able to heat up plasma electrons by interacting with them, leading to a raise in terms of electron temperature. Furthermore, the slight decrease in Li^+ density after the central box (figure 7.3) can be related to a modest increase of Li^0. This phenomenon can release a quantity of energy equal to the lithium first ionisation potential which can heat up the electrons, growing their temperature.

In figure 7.2, the temperature of neutral lithium inside the target chamber is displayed. In the central box of the VBM, where lithium evaporates, Li^0 temperature is mostly equal to the evaporation one (around 0.1 eV), while it begins

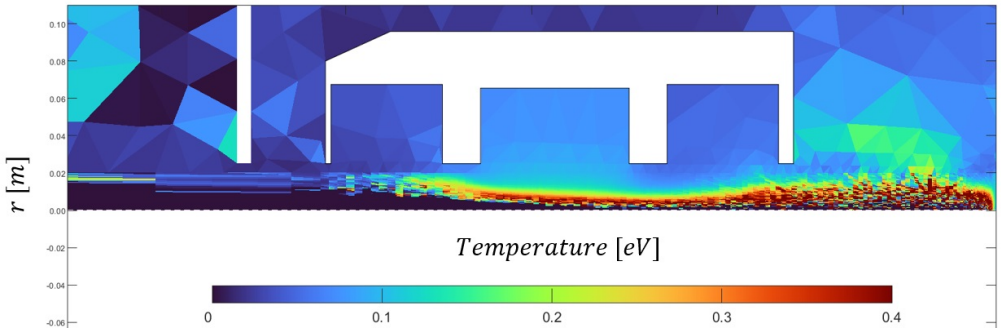

(a) Li^0 temperature

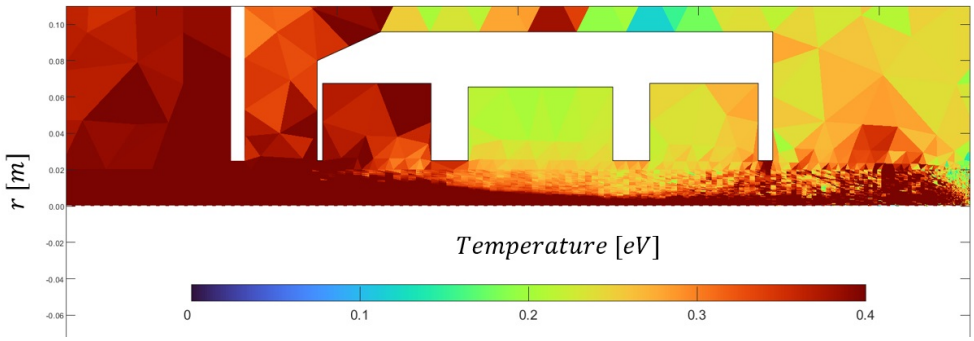

(b) H^0 temperature

Figure 7.8: Two dimensional distribution of neutral lithium and neutral hydrogen inside the target chamber

to increase when the lithium cloud interacts with the plasma beam. Hence, starting from the plasma edge, Li^0 heats up due to the several collision processes involving Li and plasma particles. Then, the temperature of neutral lithium appears to remain consistently within the range of 0.3 to 0.4 eV. In the region between the side box and the target, the same considerations made for figure 7.2 hold, as a low number of neutral particles has been simulated in this location. In addition, part of Li^0 is retained in the downstream side box. Finally, Li^0 temperature decreases in proximity of the target, where Li^+ joins the recycling phenomenon. Neutral lithium, generated by this process, reaches the thermal equilibrium with the target surface, that is at a lower temperature, and then is thermally reflected back towards the plasma beam.

7.3 Particle flux on the target

The vapor box including lithium evaporation successfully lowers the particle flux towards the target. Indeed, electron and ion (H^+ and Li^+) flux at the target location are reduced of one order of magnitude with respect to the case without Li. This behaviour is related to a global equilibrium between plasma transport, electron impact ionisation, charge-exchange, elastic collision and recombination. Although the recombination is dominant at very low temperature, this process is able to strongly contribute to the particle flux reduction because the presence of neutral particles is globally larger. Therefore, the reduction of electron and ion fluxes is directly associated with the functionality of the VBM, which serves to amplify and retain neutral particles, specifically atomic and molecular hydrogen (H^0 and H_2). Furthermore, the ionisation of the lithium cloud generates a higher number of electrons which can join the recombination process, boosting the amount of neutral particles and reducing the charged ones.
Figures 7.9 and 7.10 show the lithium effect on the VBM by plotting electron and ion fluxes at the target as a function of the radial coordinate.
Additionally, a flatter particle flux trend can be noticed in proximity of the plasma

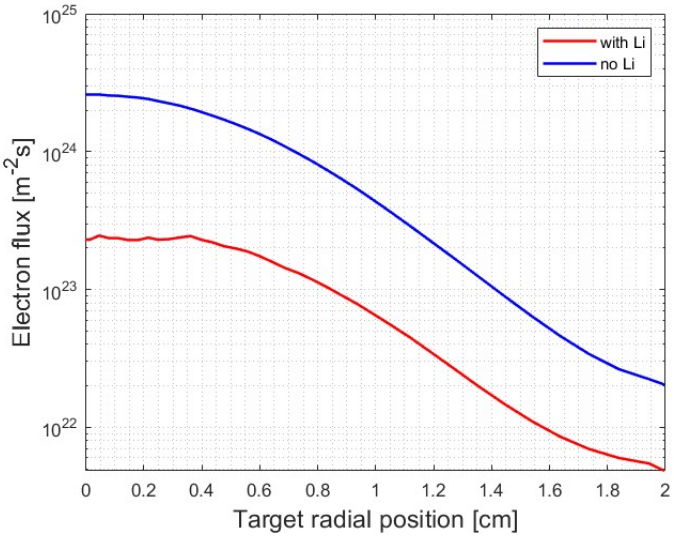

Figure 7.9: Electron flux at the target location as a function of the radial coordinate

beam centre ($r = 0$) for the model including lithium. This tendency differs form the case without Li, which depicts the peak of electron and ion fluxes in the centre of the beam, showing a half Gaussian pattern. This behaviour is explained by referring to the recycling phenomenon. Indeed, the recombination at the target

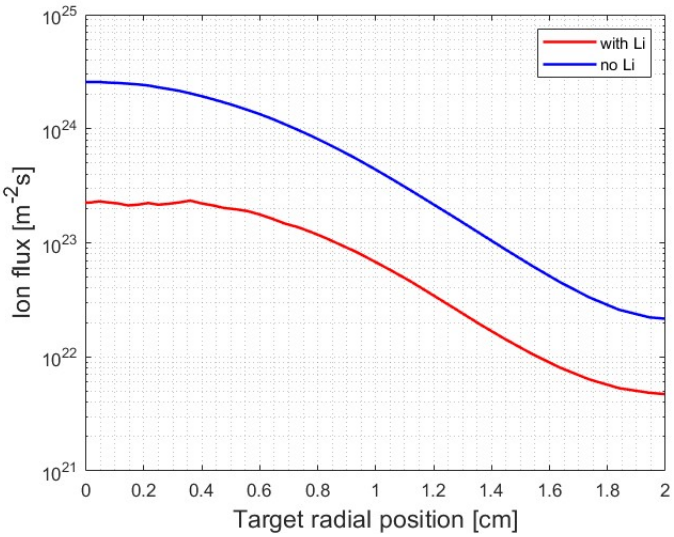

Figure 7.10: Ion flux at the target location as a function of the radial coordinate

location mostly involves Li^+ and H^+ which belong to the central part of the plasma beam where the charged particle flux is bigger.
The capability of the VBM to retain neutral particles can be also observed by looking at the neutral particle flux in proximity of the target. At this location, H^0, H_2 and Li^0 fluxes have been computed starting from the particle density and axial velocity calculated by EIRENE. Consequently, a radial interpolation has been performed for neutral fluxes along the axial coordinate and an average on the target surface has been made.
The particle flux for the different neutral species is shown in the following table.

Neutral particle fluxes averaged on the target surface $[\frac{1}{m^2 s}]$	
Neutral lithium (Li^0) flux	$1.1853 \cdot 10^{19}$
Atomic hydrogen (H^0) flux	$7.8909 \cdot 10^{18}$
Molecular hydrogen (H_2) flux	$1.3056 \cdot 10^{20}$

As evident from the data, the neutral particle flux is significantly lower (by several orders of magnitude) compared to the electron and ion flux depicted in the figures above. This indicates that the VBM is effectively fulfilling its role in retaining neutral particles, leading to an increase in plasma-neutral collisions.
Moreover, the substantial discrepancy in the particle flux suggests that the contribution of neutral particles to the heat flux at the target location is relatively modest with respect to that of ions and electrons.

7.4 Heat flux on the target

The focus of this study lies within the context of power exhaust, thus an analysis of the heat load carried by plasma particles is crucial. Additionally, understanding the distribution of heat flux at the target location is fundamental as it directly influences the behaviour of plasma-facing materials and their capacity to withstand thermo-mechanical stresses, which can affect the lifetime of the component.
Considering these factors, this section presents the heat flux at the Magnum-PSI target location. Specifically, the ion and electron heat fluxes are plotted, together with the global heat flux, as a function of the radial coordinate.
Ion and electron heat fluxes can be observed in figure 7.11. As one might anticipate, the evaporation of lithium significantly dimishes the heat flux associated with ions and electrons. Indeed, plasma interacts with the lithium cloud, resulting in the loss of momentum and energy due to intensified collision processes. Plasma expends energy to ionise neutral lithium, after which other crucial interactions, such as elastic collisions and charge-exchange, occur, thereby reducing the energy carried by the particles. These processes contribute to lowering the temperature, as the introduction of lithium corresponds to a source of friction, disrupting the conservation of plasma pressure ($p = nT$).
Reducing the plasma temperature is not sufficient to decrease the heat flux towards the target, indeed recombination is also needed. When particles recombine, the ionisation potential is released, thus the ion particle flux must be diminished to further mitigate the heat flux (see equation 4.1). This means that recombination before the target location is required. Collision processes involving lithium and neutral particles can effectively reduce the plasma temperature, thereby increasing the likelihood of particle recombination. Moreover, lithium ionisation provides additional electrons that can facilitate this process.
As it is possible to expect, particle and heat fluxes exhibit a comparable pattern. Particularly, ion and electron heat fluxes manifest the presence of a peak at a location other than $r = 0$ in the configuration involving lithium. The tendency for the maximum value of the heat flux to radially shift outward from the plasma beam centre line can be referred to as *peak shift*. This behaviour is attributed to the recycling phenomenon. Hydrogen and lithium ions originating from the central part of the beam effortlessly recombine at the target location moving the flux peak.

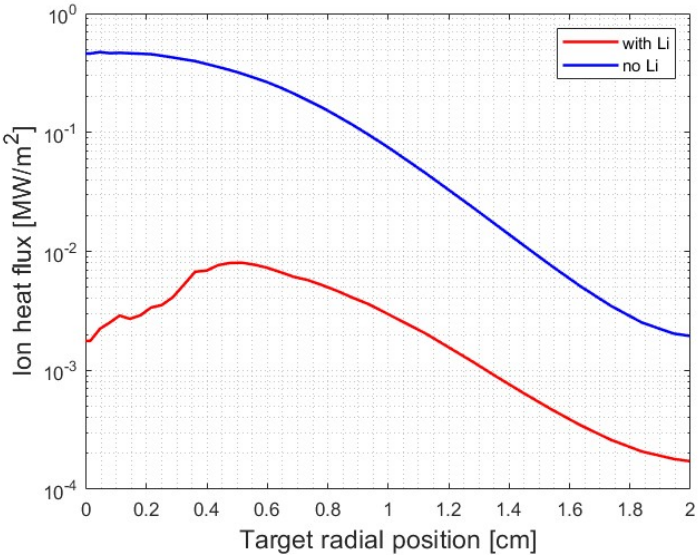

(a) Ion heat flux

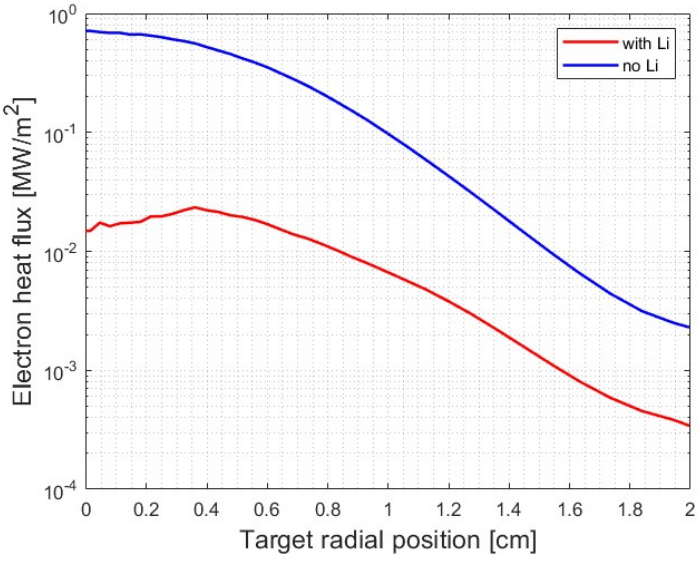

(b) Electron heat flux

Figure 7.11: Ion and electron heat flux at the target location as a function of the radial coordinate

Finally, the plot of the global heat flux is shown in figure 7.12. This quantity includes the contribution of ions, electrons and radiative processes, like Bremsstrahlung and line radiation. Also in this case, it is evident that the presence

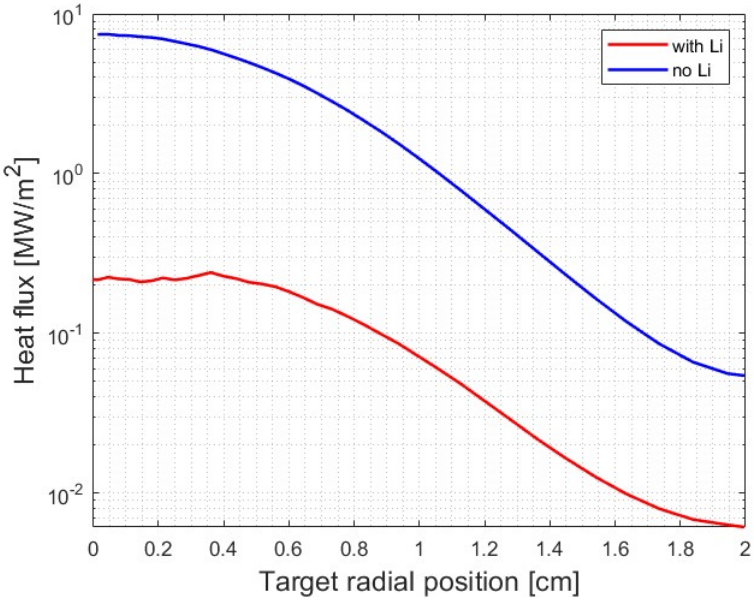

Figure 7.12: Global heat flux at the target location as a function of the radial coordinate

of lithium induces a strong reduction of the heat flux compared to the model without liquid metal.

Chapter 8

Conclusions and future perspectives

The present work focuses on the power exhaust challenge for nuclear fusion reactors. Specifically, the main concern of this thesis is related to the divertor, a key component which must be able to withstand heat and particle loads. In this specific context, scientists have extensively investigated a range of materials to determine their viability as plasma facing materials (PFMs), with liquid metals emerging as a promising candidate among the potential options. Hence, different Liquid Metal Divertor (LMD) configurations have been proposed over the years. Within these, the Vapour Box Divertor (VBD) has been selected as the main topic of this study. Particularly, a lithium Vapor Box Module (VBM), tested in the Magnum-PSI linear device, has been modelled exploiting the capabilities of the SOLPS-ITER code, which enables to study the plasma behaviour and its interaction with the device walls and lithium by coupling two different models, a fluid one for plasma particles and a kinetic transport model for neutral particles.
To accurately simulate both the device and the VBM behaviour, the process began by constructing the plasma grid, where Braginskii's equations are solved. Subsequently, all relevant properties and elements were incorporated using Divgeo, the graphical tool of SOLPS-ITER. Here, the VBM was integrated within the Magnum-PSI geometry, with careful selection of the appropriate surface designated for Li evaporation, by implementing the liquid metal particle flux. Afterwards, the temperature, wall properties, gas puffing, and pressure feedback loop (PFL) were assigned to the appropriate surfaces of the device. Then, the grid needed by the Monte Carlo code was built. In addition, modifications needed by the *input.dat* file, the main EIRENE input, were carried out. Specifically, all the collision processes including lithium have been included meticulously.

After the selection of the significant characteristics in DivGeo, the boundary conditions for the plasma domain were imposed. It is worth to mention that the electron temperature, electron density and potential profiles, necessary at the plasma source, refers to [20].
The primary goal of this study consists of investigating the capability of the lithium VBM to increase the energy and momentum transfer in order to reduce heat and particle flux to the Magnum-PSI target. Thus, simulations were performed by making a comparison between two different scenarios, with and without lithium, for the purpose to understand the impact of the metal vapor on the plasma beam. Finally, results were examined in terms of plasma and neutral particle density and temperature, while also analysing heat and particle flux on the target.
Simulations showed how lithium affects the plasma behaviour, leading to a reduction of the electron temperature, the heat flux and the particle flux.
Plasma particles start interacting with the lithium cloud in the central chamber of the VBM, where the metal is injected. Different phenomena can develop, but the charge-exchange and the electron impact ionisation are the most relevant, as these processes are able to increase the Li^+ density. Specifically, lithium shows a lower first ionisation potential compared to hydrogen. Hence, starting from the central box, Li^+ begins to dominate over plasma protons (H^+) and the species inversion phenomenon occurs. Furthermore, lithium is entrained by the plasma beam and its transport towards the target has been observed. At this location, the recycling phenomenon arises leading to an increase of the neutral lithium density.
The charge-exchange mechanism, together with the recombination, are able to boost the neutral hydrogen density. Thus, H^0 particles are retained inside the VBM resulting in an increase of the neutral particles density in this region. Additionally, atomic hydrogen can also recombine at the vapor box walls generating molecular hydrogen H_2. All these processes contribute to a strong reduction of the charged particle flux directed towards the target, impacting on the lifetime of this component.
Lithium evaporation also lowers the plasma temperature, examined in relation to the electron temperature. Indeed, plasma interacts with neutral particles (Li^0, H^0 and H_2) which are a source of friction, disrupting the pressure conservation. Collision processes increase, so energy and momentum transfer get bigger. Additionally, electrons from plasma spend energy to ionise neutral lithium, leading to a further decrease in the electron temperature. Then, plasma temperature grows due to the higher temperature of neutral lithium and atomic hydrogen retained in the downstream side box.
Lastly, the heat flux is also decreased due to the reduction of the electron temperature. However, reducing plasma temperature is not sufficient to lessen the heat flux, indeed volumetric recombination is also needed. Hence, heat flux can be diminished by lowering the ion flux. This can occur thanks to the collision

processes involving lithium and neutral particles: they effectively reduce the plasma temperature, thereby increasing the likelihood of particle recombination.
This work demonstrates the effectiveness of lithium in mitigating heat and particle loads on the Magnum-PSI target, confirming what has been observed in [20]. Nevertheless, the validation, based on the recent experiments, is still missing. This step is crucial, as it can determine the feasibility of this technology.
The experimental campaign, within the Magnum-PSI linear plasma device including the VBM, has been already carried out, recording electron and temperature profile at different distances from the Thomson Scattering in the target chamber. However, SOLPS-ITER needs the profiles in the source chamber in order to simulate the cascade-arc source of the plasma. Unluckily, these data were not registered during the experiments. Thus, taking another experimental campaign, with data coming from the Thomson Scattering at the source, could be one achievable possibility for the validation. Specifically, these experiments should depict the identical magnetic field, gas puff, and source current as observed in the experiments where the VBM has been tested. This procedure enables a comparison of density and temperature profiles, facilitating the necessary validation process. Moreover, validating the simulation serves to corroborate the potential profile, a parameter not directly derived from experimental data, but crucial for accurately representing the plasma source in SOLPS-ITER.
In conclusion, this study provides the preparation for the validation work by including all the necessary inputs and files of the code. Changing the potential, density and temperature profiles is left to a more detailed future analysis.

Bibliography

[1] Britannica. https://www.britannica.com/science/nuclear-binding-energy (cit. on p. 2).

[2] J.P. Friedberg. *Plasma Physics and Fusion Energy*. Cambridge University Press, 2007 (cit. on pp. 5–7).

[3] G.F. Nallo. «Modelling liquid metals for nuclear fusion and fission reactors». PhD thesis. Politecnico di Torino, 2021 (cit. on pp. 5, 30).

[4] Barbara Caiffi. «Neutronic Activation Analysis for ITER Fusion Reactor». In: 2014 (cit. on p. 10).

[5] C. G. Theiler. «Basic Investigation of Turbulent Structures and Blobs of Relevance for Magnetic Fusion Plasmas». PhD thesis. ÉCOLE POLYTECHNIQUE FÉDÉRALE DE LAUSANNE, 2011 (cit. on p. 16).

[6] F. Subba. *Nuclear Fusion Reactor Physics Notes*. 2021 (cit. on pp. 19, 50).

[7] M. Sala. «Numerical and Experimental studies of Plasma-Material Interaction in Linear Plasma Devices». PhD thesis. Politecnico di Milano, 2020-2021 (cit. on p. 20).

[8] P.C. Stangeby. *The Plasma Boundary of Magnetic Fusion Devices*. IOP Publishing, 2000 (cit. on p. 25).

[9] J. Safarian and T.A. Engh. «Vacuum Evaporation of Pure Metals». In: *Metallurgical and Materials Transactions* (2013) (cit. on p. 33).

[10] H.P. Summers. *The ADAS User Manual* (cit. on p. 33).

[11] T. Putterich, E. Fable, R. Dux, R.Neu, M.G. O'Mullane, and R.Wenninger. «Impurity limits in a reactor grade fusion device». In: *42nd European Physical Society Conference on Plasma Physics* (2015) (cit. on p. 33).

[12] R.J. Goldston, R. Myers, and J.A. Schwartz. «The Lithium Vapor Box Divertor». In: *Physica scripta* (2016) (cit. on p. 34).

[13] C.E. Kessel. «Overview of the Fusion Nuclear Science Facility, a Credible Breakin Step on the Path to Fusion Energy». In: *Fusion Engineering and Design* (2018) (cit. on p. 35).

[14] H.W. Kugela et al. «NSTX plasma operation with a Liquid Lithium Divertor». In: *ELSEVIER* (2011) (cit. on p. 36).

[15] R. Dejarnac. «Overview of power exhaust experiments in the COMPASS divertor with liquid metals.» In: *ELSEVIER* (2020) (cit. on p. 36).

[16] J.G.A. Scholte. «Performance of a liquid Sn divertor target during ASDEX upgrade L-mode and H-mode operation». In: *ELSEVIER* (2023) (cit. on p. 36).

[17] G. Mazzitelli et al. «Experiments on FTU with an actively water cooled liquid lithium limiter». In: *ELSEVIER* (2014) (cit. on p. 36).

[18] V.A. Evtikhin. «Experimental Study on Tokamak Plasma Interaction with Lithium Capillary-Pore Systems». In: (2002) (cit. on p. 37).

[19] T. W. Morgan. «Liquid metals as a divertor plasma-facing material explored using the Pilot-PSI and Magnum-PSI linear devices». In: *IOP Publishing* (Oct. 2017) (cit. on p. 37).

[20] J. Gonzalez, E. Westerhof, and T. W. Morgan. «SOLPS-ITER simulations of a vapour box design for the linear device Magnum-PSI». In: *Plasma Physics and Controlled Fusion* (Apr. 2023) (cit. on pp. 39, 65, 83, 84).

[21] T.W.J Driessen. *Validation of B2.5-Eunomia against Magnum-PSI Experimental Data*. 2021 (cit. on pp. 40, 62).

[22] H. J. N. van Eck. «High-Fluence and High-Flux Performance Characteristics of the Superconducting Magnum-PSI Linear Plasma Facility». In: (May 2019) (cit. on p. 41).

[23] F. Romano, V.F.B. Tanke, J. Gonzalez, J.A. Schwartz, S. Brons, R. Goldston, E. Westerhof, and T.W. Morgan. «A lithium vapour box module design for experiments in thenlinear plasma generator Magnum-PSI». In: (2021) (cit. on p. 42).

[24] J. A. Schwartz. «Experimental and modelling studies for the developmenr of the Lithium-Vapor Box Divertor». PhD thesis. Princeton University, 2020 (cit. on p. 42).

[25] I. Langmuir. «The condensation and evaporation of gas molecules». In: (1917) (cit. on p. 43).

[26] R.E. Honig. «Vapor pressure data for the solid and liquid elements». In: (1969) (cit. on p. 43).

[27] S. Braginski. «Transport processes in a plasma». In: *Reviews of Plasma Physics* (1965) (cit. on p. 45).

[28] V. Kotov, D. Reiter, and A. Kukushin. «Numerical study of the iter divertor plasma with the b2-eirene code package». PhD thesis. Institut fur Energieforschung, 2007 (cit. on p. 46).

[29] R. Schneider. «Plasma edge physics with b2-eirene». In: *Contribution to Plasma Physics* (2006) (cit. on p. 46).

[30] M. Baelmans. «Code improvements and applications of a two-dimensional edge plasma model for toroidal devices». PhD thesis. Katholieke Universiteit Leuven, 1994 (cit. on p. 46).

[31] R. Chandra. «Plasma exhaust for fusion reactors: numerical simulation and comparison with plasma beam experiments». PhD thesis. DIFFER, 2022 (cit. on p. 49).

[32] G. Dieleman. *Computer simulations of the DIFFER UPP linear plasma device*. 2023 (cit. on p. 50).

[33] *SOLPS-ITER user manual* (cit. on p. 61).

[34] B.J. Braams and H-K Chung. «Light element atom, molecule and radical behaviour in the divertor and edge plasma regions». In: *Journal of Physics* (2015) (cit. on p. 64).

[35] P.S. Krstic and D.R. Robert Schultz. «Elastic and related transport cross sections for singly charged ion–atom scattering of light metals (Li, Be, B) and hydrogen». In: *Journal of Physics* (2009) (cit. on p. 64).

[36] E.D. Marenkov, A.A. Pshenov, and A.S. Kukushin. «Shielding of liquid metal targets in plasma of linear devices». In: (2020) (cit. on p. 64).

[37] E. Tonello. *Numerical investigation of nuclear fusion relevant plasmas in linear devices through the SOLPS-ITER code*. 2017-2018.

[38] Michele Sala. *Interaction between fusion-like boundary plasmas and nanostructured tungsten*. 2016-2017.

[39] *The EIRENE Code User Manual*.